A new method to assess the possibility of brittle failure of rock induced by deep excavations

*International Journal for Numerical and Analytical Methods in Geomechanics*

WILEY

RESEARCH ARTICLE OPEN ACCESS

# A New Method to Assess the Possibility of Brittle Failure of Rock Induced by Deep Excavations

Lorenzo Milan | Monica Barbero | Mauro Borri-Brunetto

Department of Structural, Geotechnical and Building Engineering, Politecnico di Torino, Torino, Italy

**Correspondence:** Lorenzo Milan (lorenzo.milan@polito.it)

**Received:** 10 May 2024 | **Revised:** 31 December 2024 | **Accepted:** 25 January 2025

**Keywords:** brittleness index | rockburst | spalling | tunneling

## ABSTRACT

Spalling and rockburst are severe criticalities that can emerge while excavating deep tunnels in rock masses under heavy natural stress states. Here, rock brittle failure can induce massive releases of the energy stored during the excavation and dangerous projections of rock blocks into the opening. The prediction of rock brittle failure is therefore crucial and, for this purpose, different empirical brittleness indexes have been proposed in the past. However, many of them provide predictions that is often not consistent and/or truthful, as they do not consider the stress and energy variations induced in the rock mass by the excavation. This paper presents an innovative method to distinguish between ductile and brittle failure of rock around deep tunnels. The method is based on two mechanical models of rock damage that were formulated to describe brittle and ductile failure mechanisms within the rock mass, as induced by the stress release during the excavation. These models are integrated into the definition of a new brittleness index, named tunnel brittleness index (TBI). TBI quantifies the outcome of the competition between the two failure mechanisms, estimating the susceptibility of the rock mass to brittle failure. The effectiveness and the application of TBI are shown with reference to a real case study. Specifically, TBI appears as a promising and useful tool for engineers dealing with deep tunnel projects that may be employed for predicting brittle collapses in the early stages of the design, which would be crucial in the preliminary choice of excavation techniques and machinery, and the support systems.

## 1 | Introduction

In recent years, an increasing number of underground caverns and tunnels are being constructed at high depths, as the utilization of underground space is constantly increasing [1–3]. The term "deep tunnel" refers to a tunnel excavated at such a high depth below the ground, that the variations of the geostatic stresses between the crown and the invert can be assumed negligible. This condition allows one to assume homogeneous geostatic stresses acting in the rock mass before excavation, with magnitude corresponding to the values computed at the center of the future tunnel. In practice, shallow and deep tunnels are usually differentiated by the relationship between their depth ($H$) and their diameter ($D$), considering deep tunnels those with $H/D$ ranging from 3 to 10 [4, 5].

One of the main problems affecting deep tunnels is the very high natural stress, with the consequent occurrence of a significant deviatoric stress during the excavation process, leading to the failure of the rock mass. By assuming the rock mass as an equivalent continuum medium, the failure modes expected around deep tunnels can be classified into two main categories, ductile or brittle, depending on the strength and deformability properties of the material, as well as on the applied stresses.

Ductile failure induces the progressive plasticization of the rock mass surrounding the cavity, with a consequent increase in the inwards radial displacements. In some cases, the collapse of small volumes of broken material from the crown and the sidewalls into the cavity may occur, driven by gravity. As the rock mass strength does not reduce significantly after the elastic limit

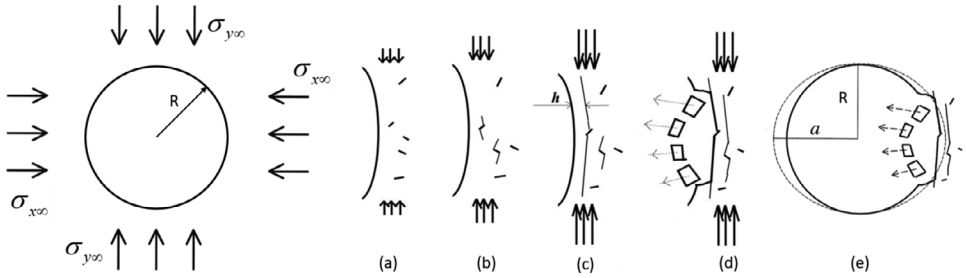


**FIGURE 1** | Schematization of the rockburst process around cavities: (a) loading beginning, (b) crack propagation initiation, (c) unstable crack propagation, (d) buckling and breaking of the rock slab, and (e) opening shape variation from circle to ellipse (modified from [32]).

is exceeded, this failure mechanism generally does not evolve rapidly over time.

On the contrary, brittle failure induces sudden and dangerous phenomena, in which the rapid fracturing and instabilization of the material are accompanied by significant energy releases, which may be more or less violent [1, 2, 6–8]. In less violent cases, slabbing and spalling phenomena occur, which produce the collapse of small-sized and low-speed rock blocks. In the most violent cases, rockburst phenomena are observed. This is a well-known problem occurring, for example, during tunneling for transportation systems, hydroelectric projects, nuclear waste disposal, and underground plants [9–15]. Different definitions have been proposed by many authors for rockburst, but a standard one has not been identified yet [15]. This phenomenon is commonly described as a dangerous event consisting of a sudden rock failure characterized by the breaking up of rock and its projection into the excavation, accompanied by a violent release of energy [8, 16–22]. Specifically, the excavation process relieves the surrounding rock of a massive pressure, and the release of energy causes the rock to fracture and explode as it attempts to reestablish a new equilibrium state [23, 24].

The projection of rock blocks into the opening may result in delays, economic losses, collapses, damage to equipment and, sometimes, casualties [14, 21, 25]. In fact, most rock blocks are ejected with velocities up to 6 m/s, while small fragments can reach velocities of about 50 m/s [15]. This kind of failure is caused by the concentration of high deviatoric stresses around the openings, which increase with depth. Moreover, rockbursts mostly occur in massive, stiff rocks, as they can store more strain energy [8, 12, 26–28].

Research activities have been focused on this phenomenon in the past. Nevertheless, the rockburst mechanism has not been fully understood yet [23, 29–31]. Germanovich and Dyskin [32] proposed a model to interpret the mechanism of rockburst in excavations, according to which brittle failure is originated by compressive failure near the free surface, due to the propagation of tensile fractures parallel to the direction of maximum compression (splitting). Specifically, crack growth initiates due to compressive stress concentration at the cavity wall, then an unstable propagation occurs, which separates a rock slab from the rock mass. Subsequently, the rock slab buckles and breaks because of tensile failure, projecting rock blocks into the opening. At this point, a new free surface is exposed and the process continues till the opening shape stabilizes, tending to an ellipse, as the crack growth runs out. Figure 1 shows a schematization of the process described.

### 1.1 | Overview on the Brittleness Indexes

Due to the serious consequences of rockburst, it is evident that the proper prediction of this phenomenon in the design and construction phases of deep tunnels is of paramount importance. One of the most used tools for estimating rockburst proneness during deep tunnel design is represented by brittleness indexes. These indexes allow one to evaluate the brittleness of the rock mass giving a predictive judgment on the probability of occurrence of a rockburst or on its magnitude.

As stated by He et al. [12], rock brittleness is one of the most important factors for the assessment of rockburst proneness. However, the definition and measurement of brittleness in rock mechanics is not standardized and many empirical approaches have been proposed in the literature. Meng et al. [33] collected more than 80 rock brittleness indexes proposed by different authors for different applications in rock mechanics. On the other hand, Zhou et al. [34] and Askaripour et al. [3] provided two comprehensive reviews of the rockburst assessment methods proposed in the literature since 1965. In these works, 65 empirical brittleness indexes for rockburst classification were collected and analyzed. In most cases, the indexes for rockburst classification are given as a function of the rock strength parameters, the stresses at the tunnel boundary, values of the energy dissipations, or strain values obtained from laboratory tests. Among the above-mentioned 65 indexes, we highlight the following four, which belong to the most used set:

- $B_I$ [35], defined as the ratio between the uniaxial compressive and tensile strengths of the rock:

$$B_I = \frac{\sigma_{c,i}}{\sigma_{t,i}} \tag{1}$$

- PES (potential energy of elastic strain [36]), function of the uniaxial compressive strength and the unloading tangential modulus of the rock:

$$PES = \frac{\sigma_{c,i}^2}{2E_s} \tag{2}$$

- $T_s$ (tangential stress index [37]), defined as the ratio between the maximum tangential stress in the rock mass surrounding

the opening and the uniaxial compressive strength of the rock:

$$T_s = \frac{\sigma_\theta}{\sigma_{c,i}} \tag{3}$$

- S [38], function of the maximum circumferential stress in the surrounding rock, the maximum principal in situ stress and the uniaxial compressive strength of rock:

$$S = \frac{\sigma_\theta + \sigma_1}{\sigma_{c,i}} \tag{4}$$

- BBR (Burst–Brittleness ratio [39]), which has the same characteristics as $B_I$, but with the substitution of $\sigma_{t,i}$ with the rock point load index (PLI) proposed by Masoumi et al. [40]:

$$\begin{aligned} BBR_d &= k\frac{A}{D^2} \text{ for diametral point loading direction} \\ BBR_a &= k\frac{A}{4LD/\pi} \text{ for axial point loading direction} \end{aligned} \tag{5}$$

where D is the equivalent diameter of the specimen, A the specimen contact area, L the length of the specimen, and k the index-to-strength conversion factor.

Some studies showed that, due to their empirical formulation, these indexes do not always provide results that are consistent with each other and/or representative of the real cases. Moreover, different rockburst hazard or intensity classifications have been proposed by different authors for the same indexes, so the classification thresholds are not uniform and difficulties arise in the application of those indexes [15].

As an example, Khanlari [30] analyzed the predictions provided by the indexes PES, $B_I$ and $T_s$ for a critical portion of the water supply Karaj–Tehran tunnel (Tehran province—Iran) and found conflicting predictions (Table 1). Moreover, Farhadian [41] analyzed the predictions provided by the indexes $W_{et}$ (proposed by Neyman et al. [42]) and $T_s$ for 28 rockburst case studies, according to two different classifications for each index. They found that in several cases the predictions were highly dependent on the classification used and did not correspond to the observations (Table 2).

It is our opinion that the main reason for these inconsistencies is that the empirical indexes do not consider the real stress and energy variations in the rock mass induced by the excavation process and by the failure mechanism. Trying to overcome these limitations and to improve the prediction of rockburst phenomena in the early design stages of deep tunnels, in this paper a novel method for distinguishing between ductile and brittle failure is proposed, based on the concept of competition between two opposite damage mechanisms. The approach is based on the analytical solution of two different mechanical models specifically developed to interpret the rock damage associated with ductile and brittle failure. Both the failure modes are assumed as driven by the stress release resulting from the excavation of a deep tunnel.

From an analytical point of view, ductile failure has been extensively studied in solving two-dimensional boundary value problems for an elastoplastic model of the rock mass, assuming it as an equivalent continuum material, within the convergence-confinement method [43–51]. The analysis deals with a circular cross-section of the tunnel and the excavation process is simulated by reducing a fictitious pressure inside the cavity, from the initial geostatic value to zero. During this reduction, the formation of a plastic zone around the excavation may occur, which contains the failed portion of the surrounding material.

As regards brittle failure, a sound analytical model was proposed by Bažant et al. [52], which assumes the rock fracturing and slab buckling mechanisms described by many authors [32, 53–55] and will be described in detail and used extensively in the present work.

The two failure models proposed in this paper refer to a cross-section of a circular tunnel, simulating the excavation process according to the confinement-convergence method. As the excavation advances, the fictitious internal pressure decreases until failure occurs in the rock mass: this is called critical pressure and two different values can be estimated, depending on the brittle or ductile behavior of the rock. This approach is applied to define a new rock brittleness index: the tunnel brittleness index (TBI), which allows the estimation of the proneness to brittle failure of the rock around deep tunnels, accounting for the stress and energy variations induced by the excavation process and by the failure mechanism. The proneness to brittle failure is provided by analyzing the prevalence of one of the failure modes over the other.

In the second part of this work, the evaluation of TBI is shown through the application to a real case study, and some considerations are drawn on the index, as well as on the possible future developments of this research.

## 2 | Failure modes of the Excavation

As mentioned, the methodology proposed to forecast the occurrence of brittle or ductile rock failure around deep excavations consists in comparing the results of two analytical models of rock damage. The main outcome of this comparison is a non-dimensional brittleness index, having a role similar to that of the limit slenderness of axially compressed columns, which describes the competition between two collapse mechanisms: plastic failure due to material yielding and sudden instability of the elastic equilibrium. Specifically, a critical value marks the boundary between the two cases, for a given axial compressive force. In the case of deep excavations, the variation of stress and energy induced in the rock mass during the excavation was considered, simulating the excavation process as a process of stress reduction at the tunnel walls. The competition between ductile and brittle failure was analyzed by identifying the kind of failure as the first one occurring during the stress reduction history.

As stated before, the excavation process is simulated by gradually reducing a fictitious internal pressure from the original geostatic value to zero, and this reduction is obtained by scaling the pressure according to an unloading parameter varying between 0 (no excavation) and 1 (excavation completed). During the

**TABLE 1** | Rockburst risk assessment for the Karaj–Tehran Tunnel according to the indexes PES [36], $B_I$ [35] and $T_s$ [37]. Modified from [30].

| Cross section | PES | Rockburst hazard | $B_I$ | Rockburst intensity | $T_s$ | Rockburst intensity |
|---|---|---|---|---|---|---|
| 1 | 1266.6 | Very high | 6 | Violent | 0.18 | No rockburst |
| 2 | 260 | Very high | 31.3 | Weak | 0.36 | Weak |
| 3 | 100 | Low | 12.5 | Violent | 0.86 | Violent |
| 4 | 100 | Low | 12.5 | Violent | 0.86 | Violent |
| 5 | 100 | Low | 12.5 | Violent | 0.81 | Violent |
| 6 | 225 | Very high | 18.8 | Strong | 0.61 | Strong |
| 7 | 100 | Low | 12.5 | Violent | 0.96 | Violent |
| 8 | 225 | Very high | 18.8 | Strong | 0.64 | Strong |
| 9 | 100 | Low | 12.5 | Violent | 0.96 | Violent |
| 10 | 225 | Very high | 18.8 | Strong | 0.68 | Strong |
| 11 | 100 | Low | 12.5 | Violent | 1.01 | Violent |
| 12 | 225 | Very high | 18.8 | Strong | 0.68 | Strong |
| 13 | 100 | Low | 12.5 | Violent | 1.01 | Violent |
| 14 | 225 | Very high | 18.8 | Strong | 0.74 | Violent |
| 15 | 225 | Very high | 12.5 | Violent | 0.81 | Violent |
| 16 | 563 | Very high | 4.6 | Violent | 0.37 | Weak |
| 17 | 225 | Very high | 7.5 | Violent | 0.54 | Strong |

**TABLE 2** | Performance of the brittleness indexes $T_s$ and $W_{et}$ for the determination of rockburst intensity for 5 cases out of the 28 analyzed by Farhadian [41], "RB" stands for "rockburst").

| | | | | Rockburst classification | | | |
|---|---|---|---|---|---|---|---|
| No. | $T_s$ | $W_{et}$ | Actual | Neyman et al. 1972 | Zhou et al. 2017 | Wang et al. 1999 | Zhao et al. 2017 |
| 3 | 0.905 | 0.88 | No RB | No RB | No RB | High RB | High RB |
| 4 | 0.931 | 0.88 | No RB | No RB | No RB | High RB | Serious RB |
| 15 | 0.275 | 5.7 | Medium RB | High RB | Medium RB | No RB | Low RB |
| 16 | 0.485 | 5.7 | Medium RB | High RB | Medium RB | Low RB | Low RB |
| 17 | 0.099 | 6.58 | Medium RB | High RB | Medium RB | No RB | No RB |

internal pressure reduction, failure can occur around the tunnel: the corresponding value of the unloading parameter is called "critical." Thus, TBI is expressed as the difference between the critical unloading parameters evaluated for brittle failure (by means of a fracture mechanics approach) and for ductile failure (with an elastoplastic approach). The discussion of the two models is the subject of the following sections.

## 2.1 | Ductile Failure

The critical value of the internal pressure associated with a ductile failure is obtained through a procedure consisting of five phases: (i) mathematical modeling of the problem; (ii) analytical computation of the stresses induced by the internal pressure variation; (iii) choice of the failure criterion, (iv) identification of the critical points on the tunnel boundary through an elasto-plastic failure analysis; (v) calculation of the critical value of the internal pressure inducing elastoplastic failure at the critical points.

The problem at hand is modeled as shown in Figure 2. A cross-section of a a deep circular tunnel is considered and the stresses in the surrounding rock mass are evaluated decreasing the magnitude of a fictitious distribution of tractions on the tunnel boundary. These forces are assumed proportional to the original stress state, to simulate the progressive advancement of the tunnel face and the corresponding reduction of the confinement effect. Specifically, they vary from the initial conditions, where they correspond to the original in situ stress, to zero, following a proportionality law with factor $\Lambda$. $\Lambda$ is an unloading parameter expressing the stress relief, and goes from 0 (initial conditions) to 1 (excavation completed). The state of stress around the tunnel is expressed as a function of $\Lambda$ and, by means of a failure criterion, it is possible to find the value of this unloading parameter corresponding to the conditions of incipient plastic failure of the rock mass.

These conditions are assumed coincident with the first plasticization of a point on the tunnel boundary, which occurs when the stresses on a point on the tunnel boundary exceed the rock

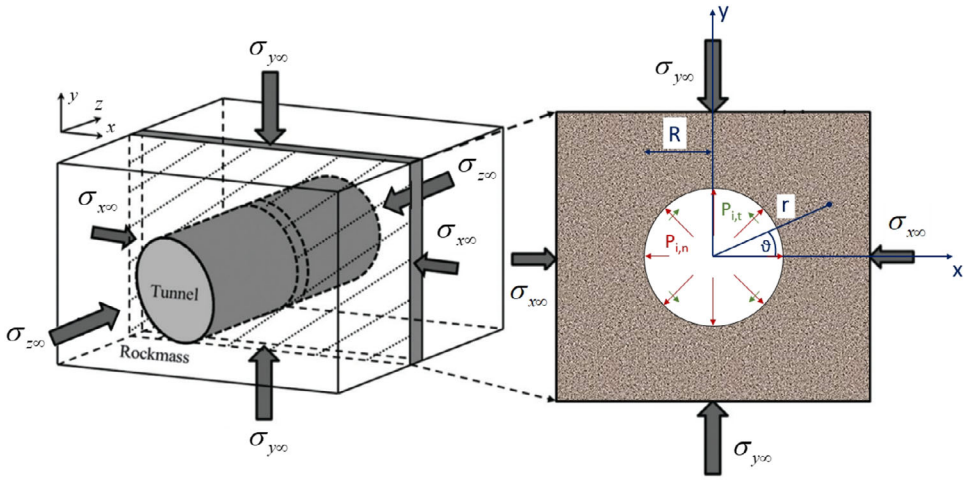


**FIGURE 2** | Reference frame and stress components for a deep tunnel in plane strain conditions (modified from [53]).

mass failure criterion. Hence, the analytical solution of the elastic problem of a circular cavity in an isotropic medium with assigned initial stress state and internal stress relief is required.

This kind of problem is quite similar to the one solved by many authors in the development of the convergence-confinement method. However, the assumptions we made are different from those of other models available in the literature.

First, we assume plane strain conditions only during the deformation process, while all the solutions found in the literature assume plane strain conditions also when determining the initial axial stress in the direction of the tunnel axis. In this paper, a geostatic stress tensor $\boldsymbol{\sigma}_\infty$ is assumed, characterized by isotropic natural stresses in the horizontal plane ($xz$). The horizontal components are defined as a function of the vertical stress, by means of the stress ratio $k$, as follows:

$$\begin{aligned} \boldsymbol{\sigma}_\infty &= \begin{pmatrix} \sigma_{x\infty} & 0 & 0 \\ 0 & \sigma_{y\infty} & 0 \\ 0 & 0 & \sigma_{z\infty} \end{pmatrix} \\ \sigma_{z\infty} &= k\sigma_{y\infty} \\ \sigma_{x\infty} &= k\sigma_{y\infty} \end{aligned} \tag{6}$$

Second, we consider an in situ stress where the coefficient $k$ may be assumed different values, depending on the geological stress history of the analyzed site. This last hypothesis has important consequences on the fictitious internal pressure and increases the mathematical complexity of the problem.

Third, a 3D failure criterion is used to consider the strength of the rock mass, allowing for the consideration of the effect of all the principal stress components on the rock mass behavior.

The stresses induced in the rock mass by the excavation process are obtained by using an approach similar to that proposed by Timoshenko and Goodier [56] to study the effect of circular holes in plates. The computation is described below.

The rock mass is considered as an infinite circular plate with radius $r = b \to \infty$, containing a circular hole with radius $R$, and the in-plane stresses on the boundary of a ring with generic radius $R < r < b$ are evaluated. With reference to Figure 2, the original stress state in the plate (no hole conditions) can be expressed using a cylindrical reference frame with the $z$ axis corresponding to the longitudinal axis of the excavated cylindrical zone and $(r, \theta)$ denoting the usual polar coordinates in the plane perpendicular to the longitudinal axis. The general expression of this state of stress can be seen as the superposition of two systems. The first one does not depend on $\theta$, namely:

$$\begin{aligned} \sigma_{r,0}^{(1)} &= \frac{\sigma_{x\infty} + \sigma_{y\infty}}{2} \\ \sigma_{\theta,0}^{(1)} &= \frac{\sigma_{x\infty} + \sigma_{y\infty}}{2} \\ \tau_{r\theta,0}^{(1)} &= 0 \end{aligned} \tag{7}$$

and the second is given by

$$\begin{aligned} \sigma_{r,0}^{(2)} &= \frac{\sigma_{x\infty} - \sigma_{y\infty}}{2}\cos(2\theta) \\ \sigma_{\theta,0}^{(2)} &= -\frac{\sigma_{x\infty} - \sigma_{y\infty}}{2}\cos(2\theta) \\ \tau_{r\theta,0}^{(2)} &= \frac{\sigma_{y\infty} - \sigma_{x\infty}}{2}\sin(2\theta) \end{aligned} \tag{8}$$

Therefore, by summing Equations (7) and (8), we obtain the components of the initial stress state within the plate:

$$\begin{aligned} \sigma_{r,0} &= \frac{\sigma_{x\infty} + \sigma_{y\infty}}{2} + \frac{\sigma_{x\infty} - \sigma_{y\infty}}{2}\cos(2\theta) \\ \sigma_{\theta,0} &= \frac{\sigma_{x\infty} + \sigma_{y\infty}}{2} - \frac{\sigma_{x\infty} - \sigma_{y\infty}}{2}\cos(2\theta) \\ \tau_{r\theta,0} &= \frac{\sigma_{y\infty} - \sigma_{x\infty}}{2}\sin(2\theta), \end{aligned} \tag{9}$$

where:

- the subscript "0" denotes the initial condition of the excavation process;
- $\sigma_{r,0}$ is the radial original stress;

**TABLE 3** | Stress systems considered to compute the effect of unloading.

| Case | Original stress | Internal stress |
|---|---|---|
| 1 | $\sigma_{r,0}^{(1)}$ | $\sigma_{r,i}^{(1)} = (1-\Lambda)\sigma_{r,0}^{(1)}$ |
| | $\tau_{r\theta,0}^{(1)}$ | $\tau_{r\theta,0}^{(1)} = 0$ |
| | $\sigma_{\theta,0}^{(1)}$ | $\sigma_{\theta,i}^{(1)} = (1-\Lambda)\sigma_{\theta,0}^{(1)}$ |
| 2 | $\sigma_{r,0}^{(2)}$ | $\sigma_{r,i}^{(2)} = (1-\Lambda)\sigma_{r,0}^{(2)}$ |
| | $\tau_{r,0}^{(2)}$ | $\tau_{r\theta,i}^{(2)} = (1-\Lambda)\tau_{r\theta,0}^{(2)}$ |
| | $\sigma_{\theta,0}^{(2)}$ | $\sigma_{\theta,i}^{(2)} = (1-\Lambda)\sigma_{\theta,0}^{(2)}$ |

- $\sigma_{\theta,0}$ is the circumferential original stress;
- $\tau_{r\theta,0}$ is the tangential original stress.

The reduction of the stress components due to the excavation process is given as a function of $\Lambda$, as reported in Table 3. For calculation purposes, it is convenient to deal separately with the two systems of stress, solving the two cases. The complete solution is found by summing the two sets of stress components obtained from the two cases.

Case 1 is solved using the axisymmetric solution proposed by Kirsch to calculate the stresses around a circular hole in an infinite elastic solid, with an isotropic original state of stress. A detailed derivation of the Kirsch equations can be found in the work of Jaeger et al. [57]. This solution provides the radial and tangential stresses at a distance $r$ from the center of a circular opening with radius $R$, considering a hydrostatic initial stress $p_0$ and an internal pressure $p_i$:

$$\begin{aligned}\sigma_r^{(1)} &= p_0 - (p_0 - p_i)\frac{R^2}{r^2}\\ \sigma_\theta^{(1)} &= p_0 + (p_0 - p_i)\frac{R^2}{r^2}\\ \tau_{r,\theta}^{(1)} &= 0\end{aligned} \tag{10}$$

In order to apply Equation (10) to the problem at hand, the following substitutions are made, introducing the stress reduction parameter $\Lambda$:

$$\begin{aligned}p_0 &= \sigma_{r,0}^{(1)}\\ p_i &= (1-\Lambda)\sigma_{r,0}^{(1)}\\ \sigma_{x\infty} &= k\sigma_{y\infty}\end{aligned} \tag{11}$$

Consequently, introducing the non-dimensional distance from the tunnel center $\rho = r/R$, the final solution to case 1 is:

$$\begin{aligned}\frac{\sigma_r^{(1)}}{\sigma_{y\infty}} &= \frac{(k+1)\left(\rho^2-\Lambda\right)}{2\rho^2}\\ \frac{\sigma_\theta^{(1)}}{\sigma_{y\infty}} &= \frac{(k+1)\left(\rho^2+\Lambda\right)}{2\rho^2}\\ \frac{\tau_{r\theta}^{(1)}}{\sigma_{y\infty}} &= 0\end{aligned} \tag{12}$$

The solution of case 2 requires the use of the Airy stress function and is obtained by solving the equilibrium and the compatibility equations of an infinite plate with a circular hole, biaxial original stress state, and internal stress relief. The complete calculation of the stresses induced by case 2 is described in Appendix A, while its final result is given by:

$$\begin{aligned}\frac{\sigma_r^{(2)}}{\sigma_{y\infty}} &= \frac{(k-1)\left[\rho^4+\Lambda\left(3-4\rho^2\right)\right]}{2\rho^4}\cos(2\theta)\\ \frac{\sigma_\theta^{(2)}}{\sigma_{y\infty}} &= \frac{-(k-1)(3\Lambda+\rho^4)}{2\rho^4}\cos(2\theta)\\ \frac{\tau_{r\theta}^{(2)}}{\sigma_{y\infty}} &= \frac{-(k-1)[\rho^4+\Lambda(2\rho^2-3)]}{2\rho^4}\sin(2\theta)\end{aligned} \tag{13}$$

Finally, the in-plane stresses on the boundary of a ring with non-dimensional radius $\rho = r/R$ as a function of $\Lambda$ are computed, summing the effects of case 1 (Equation 12) and case 2 (Equation 13) and obtaining:

$$\begin{aligned}\frac{\sigma_r}{\sigma_{y\infty}} &= \frac{(k+1)(\rho^2-\Lambda)}{2\rho^2} + \frac{(k-1)\left[\rho^4+\Lambda(3-4)\rho^2\right]}{2\rho^4}\cos(2\theta)\\ \frac{\sigma_\theta}{\sigma_{y\infty}} &= \frac{(k+1)(\rho^2+\Lambda)}{2\rho^2} - \frac{(k-1)(3\Lambda+\rho^4)}{2\rho^4}\cos(2\theta)\\ \frac{\tau_{r\theta}}{\sigma_{y\infty}} &= -\frac{(k-1)[\rho^4+\Lambda(2\rho^2-3)]}{2\rho^4}\sin(2\theta)\end{aligned} \tag{14}$$

For the determination of the out-of-plane stress component, $\sigma_z$, plane strain conditions are assumed during the deformation process associated to the variation of $\Lambda$ from 0 to 1. In this case, the variation of $\sigma_z$ is linked to the variations of the in-plane stresses:

$$\begin{aligned}\Delta\sigma_z &= \nu(\Delta\sigma_r + \Delta\sigma_\theta) = \nu(\sigma_r - \sigma_{r,0} + \sigma_\theta - \sigma_{\theta,0})\\ &= \nu(\sigma_r + \sigma_\theta) - \nu(\sigma_{r,0} + \sigma_{\theta,0})\end{aligned} \tag{15}$$

where $\nu$ is the Poisson's ratio.

While analyzing the right side of Equation (15), it can be noted that the sum $\sigma_{r,0} + \sigma_{\theta,0}$ is not dependent on $\theta$:

$$\sigma_{r,0} + \sigma_{\theta,0} = \sigma_{y\infty}(1+k) \tag{16}$$

Moreover, the sum $\sigma_r + \sigma_\theta$ can be computed using Equation (14), obtaining:

$$\sigma_r + \sigma_\theta = \sigma_{y\infty}\left(k+1-\frac{2\Lambda(k-1)\cos(2\theta)}{\rho^2}\right) \tag{17}$$

Therefore, the total out-of-plane stress as a function of $R$, $\theta$ and $\Lambda$ is written as:

$$\sigma_z = \sigma_{z,\infty} + \Delta\sigma_z = \sigma_{y\infty}\left[k - \frac{2(k-1)}{\rho^2}\nu\Lambda\cos(2\theta)\right] \tag{18}$$

In order to calculate the critical unloading parameter which induces ductile failure (called $\Lambda_{duc}$), the stress paths at the points on the tunnel boundary (i.e., for $\rho = 1$) where failure first occurs, expressed as functions of $\Lambda$, are then compared with the rock strength.

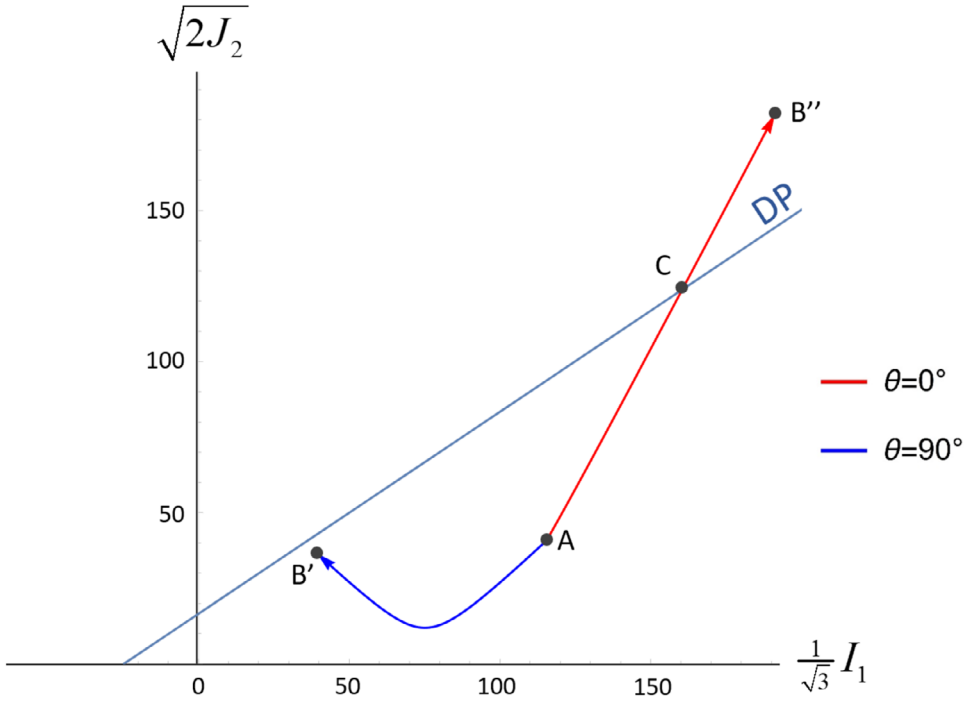


**FIGURE 3** | Illustrative representation of the stress paths at the sidewall ($\theta = 0°$) and at the crown ($\theta = 90°$) on the Rendulic plane. The line with positive slope and labeled "DP" is the Drucker–Prager failure envelope evaluated assuming $A = 12$ MPa, $B = 0.3$, $\sigma_{x\infty} = 100$ MPa and $k = 0.5$. The stress paths are drawn for $\Lambda$ ranging between 0 (point $A$) and 1 (points $B'$ and $B''$). The stress path at the sidewall crosses the failure envelope for a certain value of $\Lambda$ (point $C$), corresponding to failure conditions.

To take into account also the effect of $\sigma_z$, which is not always the intermediate principal stress, the three-dimensional Drucker–Prager failure criterion is chosen, written in the form:

$$\sqrt{J_2} = A + BI_1 \tag{19}$$

where $J_2$ represents the second invariant of the deviatoric part of the Cauchy stress tensor, $I_1$ denotes the first invariant of the Cauchy stress tensor, and $A$ and $B$ are strength parameters. This criterion can be visualized on the Rendulic plane (see Figure 3), where it appears as a straight line, and the intersections between this line and the stress path associated with points along the tunnel boundary indicate failure conditions.

As a result, the Drucker–Prager failure criterion for a point on the tunnel boundary, as a function of $\sigma_{y\infty}$, $A$, $B$, $k$, and $\Lambda$, can be written as:

$$-6P_0 - P_1 + \sqrt{3}\sqrt{(P_2 + P_3 + P_4 + P_5)} = 0 \tag{20}$$

where $P_0 = A/\sigma_{y\infty}$, while $P_1, P_2, P_3, P_4$, and $P_5$ are functions of $\Lambda$, $k$, $A$ $B$, $\nu$, and $\theta$, the expressions of which are given in Appendix B.

The parameters $A$ and $B$ can be expressed in terms of the tensile ($\sigma_{t,rm}$) and compressive ($\sigma_{c,rm}$) strengths of the rock mass, as follows:

$$A = \frac{2}{\sqrt{3}}\left(\frac{\sigma_{c,rm} \cdot \sigma_{t,rm}}{\sigma_{c,rm} + \sigma_{t,rm}}\right)$$
$$B = \frac{1}{\sqrt{3}}\left(\frac{\sigma_{c,rm} - \sigma_{t,rm}}{\sigma_{c,rm} + \sigma_{t,rm}}\right) \tag{21}$$

These expressions are obtained by applying the failure criterion to the cases of uniaxial compression or tension, considering the compressive stresses positive.

To relate a value of $\Lambda$ with a failure condition, the value of the Drucker–Prager function is evaluated at the points of the tunnel boundary following their stress paths. The points that fail for the smallest value of $\Lambda$, for a given set of parameters, are called "critical points." To proceed with the analysis, their position has to be found.

Due to the complexity of the analytical computations, the critical points are found by a numerical analysis. For this purpose, a Matlab routine was developed, which computes the $\Lambda$ values satisfying the Drucker–Prager function (so they are associated with incipient failure conditions) for a high number of combinations of the governing variables ($k, P_0, B, \theta, \nu$).

Specifically, 584,988 combinations were analyzed, obtained from the following values of the input parameters:

- 6 equally spaced values between 0.1 and 0.49 for $\nu$;
- 20 equally spaced values between 0.0001 and 20 for $P_0$;
- 11 equally spaced values between 0 and 1 for $k$ (the cases of $k > 1$ can be treated as cases of $0 < k < 1$ by operating a 90° rotation of the reference system);
- 11 equally spaced values between 0 and $\frac{\sqrt{3}}{3}$ for $B$. The maximum value ($B = \frac{\sqrt{3}}{3}$) is the maximum of the function that links $B$ to the friction angle, $\varphi$, of the material ($B = \frac{2\sin\varphi}{\sqrt{3}(3-\sin\varphi)}$), with $\varphi$ ranging from 0° to 90°;

- 41 equally spaced values between 0° and 90° for $\theta$ (exploiting the symmetry of the problem).

In none of the cases analyzed was the minimum critical $\Lambda$ value (corresponding to failure) recorded for $\theta$ values other than 0° or 90°. The critical points proved to be always the crown or the sidewall, for any initial condition (i.e., for any combination of $k, P_0, B, \nu, \theta$). Therefore, it is reasonable to assume that the critical points of the tunnel boundary are always the crown or the sidewall.

The critical value of $\Lambda$ associated with ductile failure at the critical points can be calculated analytically. To do this, the $\Lambda$ values satisfying the Drucker–Prager criterion are computed, obtaining $\Lambda_{duc,c}$ for the crown and $\Lambda_{duc,s}$ for the sidewall. A double solution is obtained in both cases and, being $0 < \Lambda < 1$, the minimum positive one is considered. Then, the minimum between the two $\Lambda$ values is selected as the critical ductile $\Lambda$ value, $\Lambda_{duc}$, that is:

$$\Lambda_{duc} = \min[\min(\langle \Lambda_{duc,s} \rangle); \min(\langle \Lambda_{duc,c} \rangle)] \tag{22}$$

where $\langle \bullet \rangle$ denotes the positive part of $\bullet$. The complete solution of this procedure is reported in Appendix C.

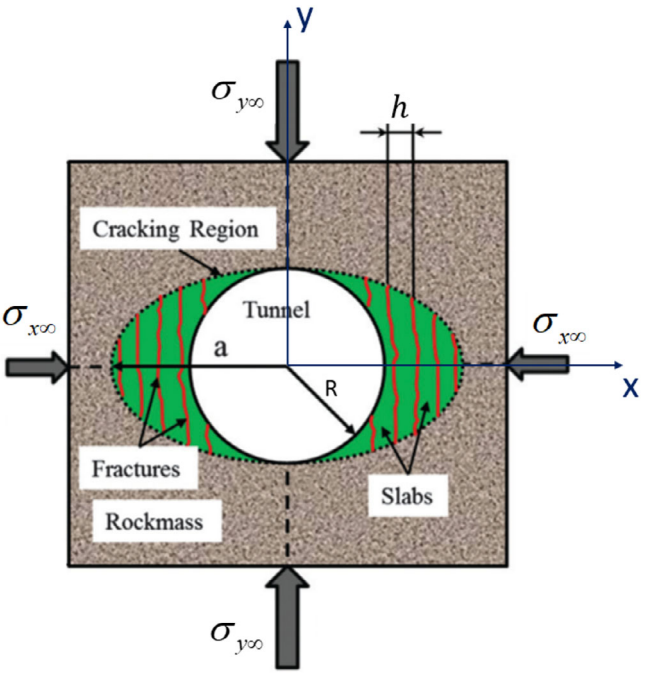


**FIGURE 4** | Cracking region containing vertical rock slabs and enlarging the circular cavity into an ellipse (modified from [53]).

## 2.2 | Brittle Failure

A description of the process of brittle failure of deep excavations in hard rocks is provided by fracture mechanics. In this approach, a mechanism of cavity instability is considered as driven by the unstable propagation of fractures in the direction of maximum compression and by the slab buckling process, as assumed in the model proposed by Germanovich and Dyskin [32], previously described.

Bažant et al. [52] proposed a 2D analytical model to describe the failure of circular cavities in plane strain conditions in an isotropic linear elastic medium, based on the assumption that regions of parallel equidistant splitting cracks form at the sides of the cavity. This leads to rock slabs that separate from the rock mass, which are assumed to buckle as slender columns (Figure 4). The model was originally developed to study borehole breakouts, but was also applied to underground openings [53, 58–60].

This model allows the computation of the geostatic in-plane stresses inducing collapse, assuming that: (i) the rock slabs which form at the side of the cavity have constant height and buckle simultaneously; (ii) buckling of the rock slabs is resisted by both their bending stiffness and the shear stresses mobilized along the fractures; (iii) an energy balance holds between the energy release associated with the formation of the cracking region and the energy dissipation due to the propagation of the cracks. All the computations involved in the model are performed assuming that the cavity has been completely excavated (i.e., $\Lambda = 1$), so no fictitious internal pressure is accounted for and the excavation process is not considered.

In the present work, this model was expanded to account for the effect of the progressive excavation process, simulated through the usual reduction of the fictitious internal pressure inside the cavity. The resulting model can be used to determine a critical value of $\Lambda$ corresponding to brittle failure initiation, $\Lambda_{brt}$.

As in the case for the determination of $\Lambda_{duc}$, a circular cavity of radius $R$ in an infinite elastic space is considered, subjected to the geostatic stress $\boldsymbol{\sigma}_\infty$ (Equation 6). According to the original model by Bažant et al. [52], the brittle failure process consists of the formation of a region of equidistant cracks parallel to the direction of maximum compression, which collapses enlarging the cavity into an ellipse with semi-axes $R$ and $a > R$ (Figure 4).

The first step of the calculation of $\Lambda_{brt}$ is to compute the variation in the potential energy per unit thickness in the out-of-plane direction, due to the excavation of an elliptical cavity in the elastic medium. This operation is performed using the Eshelby's solutions, describing the effect of inclusions embedded in an elastic continuum [61].

The initial rock mass is considered as an elastic space subjected to the original stress state $\boldsymbol{\sigma}_\infty$. A certain deformation $\boldsymbol{\epsilon}^*$ (called eigenstrain) is then applied to the ellipse corresponding to the contour of the future enlarged tunnel (the collapse of the slabs enlarges the cavity into an ellipse), such that the final stress state in the area bounded by the elliptical contour is zero. This means that $\boldsymbol{\epsilon}^*$ must be such to induce in the ellipse a stress state equal to $-\boldsymbol{\sigma}_\infty$. This stress, summed to the original one, makes the stress inside the ellipse equal to zero, so the material inside the ellipse can be removed without modifying the stresses and deformations of the surrounding one. As a consequence, the variation in the potential energy per unit thickness due to the excavation of an elliptical cavity in the elastic body can be computed as the energy variation due to the application of $\boldsymbol{\epsilon}^*$.

The $\epsilon^*$ components are calculated according to the Eshelby's solutions for plane strain conditions described by Mura [61] (page 81, Equation 11.22.1):

$$\sigma_x = \frac{G}{1-\nu}\left\{\left[-2+\frac{R}{a+R}+\frac{2aR+R^2}{(a+R)^2}\right]\epsilon_x^* + \left[\frac{R^2}{(a+R)^2}-\frac{R}{a+R}\right]\epsilon_y^* - \left[\frac{2a\nu}{a+R}\right]\epsilon_z^*\right\}$$

$$\sigma_y = \frac{G}{1-\nu}\left\{\left[\frac{a^2}{(a+R)^2}-\frac{a}{a+R}\right]\right\}\epsilon_x^* + \left[-2+\frac{a}{a+R}+\frac{a^2+2aR}{(a+R)^2}\right]\epsilon_y^* - \left[\frac{2R\nu}{a+R}\right]\epsilon_z^*$$

$$\sigma_z = \frac{G}{1-\nu}\left\{\left[\frac{2a\nu}{a+R}\right]\epsilon_x^* - \left[\frac{2R\nu}{a+R}\right]\epsilon_y^* - 2\epsilon_z^*\right\} \quad (23)$$

where $\sigma_x$, $\sigma_y$ and $\sigma_z$ are the non-zero components of the stress tensor inside the cavity boundary, $\boldsymbol{\sigma}$, for a given value of $\Lambda$, while $\nu$ and $G$ are the Poisson's ratio and the shear modulus of the rock mass, respectively.

In the original model by Bažant et al. [52], the stress components in Equation (23) are the geostatic ones, as no gradual excavation process is considered (i.e., no fictitious internal pressure is applied). In our model, to simulate the gradual excavation process, a force distribution on the boundary of the future cavity directed outwards must be considered to account for the effect of the fictitious internal pressure, having the same form assumed in the calculation of $\Lambda_{\text{duc}}$.

Moreover, as in the original model, the vertical stress component inside the region between the ellipse and the initial circle is reduced up to a critical value $\sigma_{\text{cr}}$, rather than to zero. In fact, as stated by Bažant et al. [52], a complete unloading cannot be assumed in the case of compression fracturing of rocks, because, upon reaching a critical value, splitting cracks form parallel to the direction of maximum compression, generating rock slabs between the initial circular boundary of the tunnel and the elliptical boundary, that are susceptible to buckling when loaded by $\sigma_{\text{cr}}$.

The critical value $\sigma_{\text{cr}}$ was determined by Bažant et al. [52] considering that the stress that can be carried by the rock slabs is limited by elastic buckling and that the opening of compression splitting cracks is null. This last condition means that adjacent rock slabs are subjected to shear stresses $\tau$ along the crack faces, and relative shear displacements, $\Delta$, occur during the slabs deflections. The value of $\sigma_{\text{cr}}$ is given by:

$$\sigma_{cr} = \frac{h^2\pi^2 E'}{12R^2w^2} + \frac{G_i h}{\lambda} \quad (24)$$

where: $E' = \frac{E}{1-\nu^2}$, $E$ is the Young's modulus and $\nu$ the Poisson's ratio of the rock mass; $h$ is the slabs thickness; $G_i$ is the shear modulus of the intact rock; $w$ is the relative wavelength, an empirical positive constant smaller than 1 such that $wR = L$ is the half-length of the splitting cracks; $\lambda$ is an equivalent thickness of the material, described in Bažant et al. [52] as "the thickness of an intact rock layer whose elastic shear relative displacement due to unit shear stress is the same as that between the crack faces." Specifically, $\lambda$ is defined as the ratio between the shear modulus of the intact rock, $G_i$, and the shear stiffness of the fractures separating the rock slabs, $k_s = \tau/\Delta$.

Based on the aforementioned approach, the components of $\boldsymbol{\sigma}$ that appear in Equation (23) are calculated as:

$$\begin{aligned}\sigma_x &= -(\sigma_{x\infty} + T_{xx})\\ \sigma_y &= -(\sigma_{y\infty} + T_{yy}) + \sigma_{\text{cr}}\\ \sigma_z &= -[\sigma_{z\infty} + \nu(T_{xx} + T_{yy} - \sigma_{\text{cr}})]\end{aligned} \quad (25)$$

where $T_{xx}$ and $T_{yy}$ are the horizontal and vertical components of the stress induced inside the ellipse by the forces distributed along its boundary. The detailed computation of $T_{xx}$ and $T_{yy}$ is described in Appendix D. The final result is given by:

$$\begin{aligned}T_{xx} &= \frac{(\lambda-1)}{8(\nu-1)}\sigma_{y\infty}\{1-5k-4\nu(1-k)-e^2[\nu(k+1)-k]\}\\ T_{yy} &= \frac{(\lambda-1)}{8(\nu-1)}\sigma_{y\infty}\{k-5+4\nu(1-k)+e^2[\nu(k+1)-1]\}\end{aligned} \quad (26)$$

Substituting these values into Equation (25), the stress components to be used in Equation (23) become known quantities, and the $\epsilon^*$ components can be evaluated by solving the system. The complete expressions are reported in Appendix E.

The knowledge of the eigenstrain $\epsilon^*$ allows one to compute the variation of the potential energy induced by the gradual excavation of an elliptic domain $\Omega$ from an infinite elastic body, considering vertical surface tractions on the elliptic boundary corresponding to $\sigma_{\text{cr}}$. The complete result of this operation is shown in Appendix F, while the equation used for the computation is:

$$\Delta\Pi_1 = -\frac{1}{2}\int_\Omega \boldsymbol{\sigma}^T\boldsymbol{\epsilon}^* dV - \int_\Omega \boldsymbol{\sigma}_0^T\boldsymbol{\epsilon}^* dV - \Psi V \quad (27)$$

where:

$$\boldsymbol{\sigma}_0 = \begin{pmatrix}\sigma_{x\infty}+T_{xx} & 0 & 0\\ 0 & \sigma_{y\infty}+T_{yy} & 0\\ 0 & 0 & \sigma_{z\infty}+\nu(T_{xx}+T_{yy})\end{pmatrix} \quad (28)$$

$$\Psi = \frac{1}{2E}[\bar{\sigma}_1^2+\bar{\sigma}_2^2+\bar{\sigma}_3^2-2\nu(\bar{\sigma}_1\bar{\sigma}_2+\bar{\sigma}_1\bar{\sigma}_3+\bar{\sigma}_2\bar{\sigma}_3)]$$

$V = \pi aR$ is the volume per unit thickness of the cavity and $\Psi$ is the elastic strain energy density stored in the ellipse, representing the strain work of the material inside the elliptic boundary up to the stress state described by $\bar{\boldsymbol{\sigma}} = \boldsymbol{\sigma} + \boldsymbol{\sigma}_0$. Hence, $\bar{\sigma}_1$, $\bar{\sigma}_2$, and $\bar{\sigma}_3$ are the non-zero components of $\bar{\boldsymbol{\sigma}}$ (i.e., the principal stresses).

The change of potential energy for a circular cavity, $\Delta\Pi_0$, comes from Equation (27) by setting $a = R$, and its complete formulation is reported in Appendix G.

The residual strain energy per unit thickness in the region between the ellipse and the initial circle (given by the bending

energy of the rock slabs) is, according to Bažant et al. [52]:

$$\Pi_{cr} = \frac{\pi(a-R)R}{2E'}\left(\frac{h^2\pi^2E'}{12R^2w^2} + \frac{G_i h}{\lambda}\right)^2 \tag{29}$$

By definition, the energy dissipation per unit thickness due to rock fracturing is:

$$\Delta W_f = \frac{\mathcal{G}_f\left(a\pi R - \pi R^2\right)}{h} \tag{30}$$

where $\mathcal{G}_f$ is the fracture energy of the intact rock.

Hence, the energy variation caused by the passage from a circular cavity in intact rock to an elliptical cavity with damaged zones containing splitting cracks is:

$$\Delta\Pi = \Delta\Pi_1 - \Delta\Pi_0 + \Pi_{cr} \tag{31}$$

The complete result of this calculation is reported in Appendix H.

To sustain the development of the fractures, described by the increase of the ellipse semi-axis $a$, the energy release rate must be equal to the dissipated energy increment, as required by the principle of conservation of energy (Bažant et al. [52]):

$$-\frac{\partial\Delta\Pi}{\partial a} = \frac{\partial\Delta W_f}{\partial a} \tag{32}$$

While computing the left side of Equation (32), as reported in Appendix I, all the terms depending on the geostatic stress components can be collected, to define the effective stress $\sigma_{ef}$. It represents a function of the stress state (which is itself a function of the geostatic stress components and $\Lambda$) corresponding to failure conditions and its computation requires the definition of the slabs thickness, $h$. Its complete expression is shown in Appendix J. We note that $\sigma_{ef}$ represents a generalization of the homonymous term introduced in the original model by Bažant et al. [52].

At failure initiation, the excavation is circular, so that $a = R$ and Equation (32), gives the following failure condition:

$${\sigma_{ef}}^2 = \frac{2\mathcal{G}_f E'}{h} + 5\left(\frac{h^2\pi^2E'}{12R^2w^2} + \frac{G_i h}{\lambda}\right)^2 \tag{33}$$

Bažant et al. [52] showed that rock fracturing occurs at the lowest possible compressive stress, meaning that the $h$ value which minimizes $\sigma_{ef}^2$ is to be considered, so the following condition must hold true:

$$\frac{\partial}{\partial h}\left[\frac{2\mathcal{G}_f E'}{h} + 5\left(\frac{h^2\pi^2E'}{12R^2w^2} + \frac{G_i h}{\lambda}\right)^2\right] = 0$$

which leads to:

$$\frac{5h^5\pi^4E'^2}{72R^4w^4} + \frac{5G_i h^4\pi^2E'}{4R^2w^2\lambda} + \frac{5G_i^2h^3}{\lambda^2} - \mathcal{G}_f E' = 0 \tag{34}$$

Equation (34) is a fifth-degree polynomial equation for $h$ that cannot be solved analytically. To overcome this difficulty, Bažant et al. [52] proposed to use the asymptotic solutions for small and large cavities, which can be easily calculated. As suggested by Qiu et al. [53], who applied the original Bazant's model to deep excavations, deep tunnels can be treated as large cavities, so the asymptotic solution of Equation (34) for large $R$ values can be used. With this assumption, the first two terms of Equation (34) can be neglected, so the slab thickness is obtained by solving a third-degree equation, whose only positive root is:

$$h = \sqrt[3]{\frac{\mathcal{G}_f E'\lambda^2}{5G_i^2}} \tag{35}$$

By substituting Equation (35) into Equation (33), an equation for $\Lambda$ is obtained, whose solution is the critical value $\Lambda_{brt}$. The complete result of this operation is shown in Appendix K.

## 3 | New Brittleness Index

The proposed TBI, which measures the proneness to ductile or brittle failure of the tunnel is defined as the difference between the two unloading parameters $\Lambda_{duc}$ and $\Lambda_{brt}$:

$$\mathrm{TBI} = \Lambda_{duc} - \Lambda_{brt} \tag{36}$$

TBI ranges from −1 to 1, and its absolute value measures the prevalence of one of the failure modes over the other. The output of the calculations falls into one of the following cases:

- The value TBI = 0 corresponds to the condition $\Lambda_{brt} = \Lambda_{duc}$, which means that the tunnel failure occurs for the same $\Lambda$ value regardless of the failure mode. Failure occurs but it is not possible to predict its kind.
- TBI > 0 implies that $\Lambda_{brt} < \Lambda_{duc}$, so that, during the excavation process, brittle failure occurs before ductile failure.
- TBI < 0 implies that $\Lambda_{brt} > \Lambda_{duc}$, so that ductile failure occurs before brittle failure.

A Matlab routine was written to calculate the TBI value as a function of the 9 input parameters shown in Table 4. The development of this routine[1] also made it possible to manage some critical situations associated with particular $\Lambda_{duc}$ and $\Lambda_{brt}$ values. In fact, from the calculations, it may result that one of the two $\Lambda$ values (or even both) takes on inadmissible values, such as greater than 1, negative or imaginary, which have no physical meaning. These situations correspond to a combination of the input parameters for which the analyzed failure mechanisms do not occur. In particular:

- If $\Lambda_{duc}$ is inadmissible and $\Lambda_{brt}$ is valid, the value TBI = 1 is forced, denoting the maximum prevalence of the brittle failure mechanism over the ductile one. This condition corresponds to the maximum brittleness of the rock-tunnel system.
- If $\Lambda_{brt}$ is inadmissible and $\Lambda_{duc}$ is valid, the value TBI = −1 is forced, denoting the maximum prevalence of the ductile failure mechanism over the brittle one. This condition corresponds to the maximum ductility of the rock-tunnel system.
- The case in which both $\Lambda_{duc}$ and $\Lambda_{brt}$ are inadmissible is handled by forcing TBI = NaN (Not a Number). This is a

**TABLE 4** | Input parameters for the calculation of TBI.

| Parameter groups | Parameter | Description |
|---|---|---|
| 1- Rock parameters | $E$ | Young's modulus of the rock mass |
| | $\nu$ | Poisson's ratio of the rock mass |
| | $\lambda$ | Equivalent thickness of the rock |
| | $A$ | Strength parameter of the Drucker–Prager failure criterion of the rock mass |
| | $B$ | Strength parameter of the Drucker–Prager failure criterion of the rock mass |
| | $G_i$ | Intact rock shear modulus |
| | $\mathcal{G}_f$ | Intact rock fracture energy |
| 2- Stress state | $\sigma_{y\infty}$ | Maximum principal geostatic stress |
| | $k$ | In situ stress ratio |

situation in which failure is not predicted by either of the two damage models used, so the TBI index is not applicable.

This computation algorithm is depicted in the flow chart shown in Figure 5.

### 3.1 | Input Parameters

As written above, the brittleness index presented in this paper depends on 9 input parameters; in this section, some useful indications are given for their choice.

$\sigma_{y\infty}$ and $k$ describe the geostatic stress state acting in the rock mass and can be obtained by in situ tests (for example flat jack tests, plate tests, etc.).

The Poisson's ratio of the rock mass, $\nu$, can be assumed equal to that of the intact rock, $\nu_i$, which can be obtained from unconfined compression tests on rock samples from in situ coring.

The Young's modulus of the rock mass, $E$, can be derived from in situ tests or by means of the empirical formulas provided in literature as a function of the rock mass quality indexes [62–65].

The strength parameters of the rock mass $A$ and $B$ can be computed using their relationship with the rock mass uniaxial compressive and tensile strengths (Equation 21). Such values can be obtained by the empirical relationships provided in literature to derive the strength parameters of the rock mass from those of the intact rock [64].

The shear modulus of the rock mass, $G_i$, can be computed as a function of $E$ and $\nu$, as follows:

$$G_i = \frac{E}{2(1+\nu)} \tag{37}$$

Since the quantification of the fracture energy, $\mathcal{G}_f$, of the rock may be difficult in certain cases, an empirical relationship useful for its determination can be used. As is known, the fracture energy, $\mathcal{G}_f$, of the intact rock is related to the fracture toughness, $K_{IC}$:

$$\mathcal{G}_f = \frac{K_{IC}}{E'} \tag{38}$$

and $K_{IC}$ can be estimated by means of empirical formulas available in the literature. Among them, the one proposed by Zhang [66] is considered particularly useful and accurate, as it improves upon the one previously provided by Whittaker et al. [67], being based on a larger and more diverse dataset of experimental results. In detail, it gives $K_{IC}$ as a function of the uniaxial tensile strength of the intact rock ($\sigma_{t,i}$):

$$K_{IC}\,[\mathrm{MPa}\cdot m^{1/2}] = 0.1453 \cdot \sigma_{t,i}\,[\mathrm{MPa}] \tag{39}$$

This relationship was used by Qiu et al. [53] when applying the model of Bažant et al. [52], and has also been used in the application presented in this paper.

Finally, the parameter $\lambda$ (introduced by Bažant et al. [52] and defined as the ratio between the shear modulus of the intact rock, $G_i$, and the shear stiffness of the splitting fractures, $k_s$) is affected by great uncertainty and its accurate determination is rather difficult, especially in the forecasting phase.

Three approaches have been suggested by various researchers to determine this parameter, which differ in the evaluation of the shear stiffness of the fractures that generate the rock slabs, $k_s$. In their initial study, Bažant et al. [52] proposed a technique to evaluate $\lambda$ by assuming a similarity in the shear behavior of rock and concrete fractures. Subsequently, Exadaktylos and Tsoutrelis [58] and Qiu et al. [53] introduced two alternative approaches, relying on laboratory tests on hollow specimens and the analysis of real splitting fracture surfaces, respectively. However, the application of these last two methods is difficult in the predictive phase of tunnel design, requiring complex operations of sampling, specimen preparation, and complex laboratory activities. As a consequence, the approach proposed by Bažant et al. [52] remains, for now, the simplest to employ for the estimation of $\lambda$ in the preliminary stages of a tunnel design, even if its results appear quite questionable.

Therefore, it is deemed important and necessary to develop a more accurate and reliable, yet simple, method for the estimation of $\lambda$. This consideration is the basis for one of the planned activities in the future developments of the research described here, aimed precisely at the search for such a method and the creation of a database of $\lambda$ values for different lithotypes, based

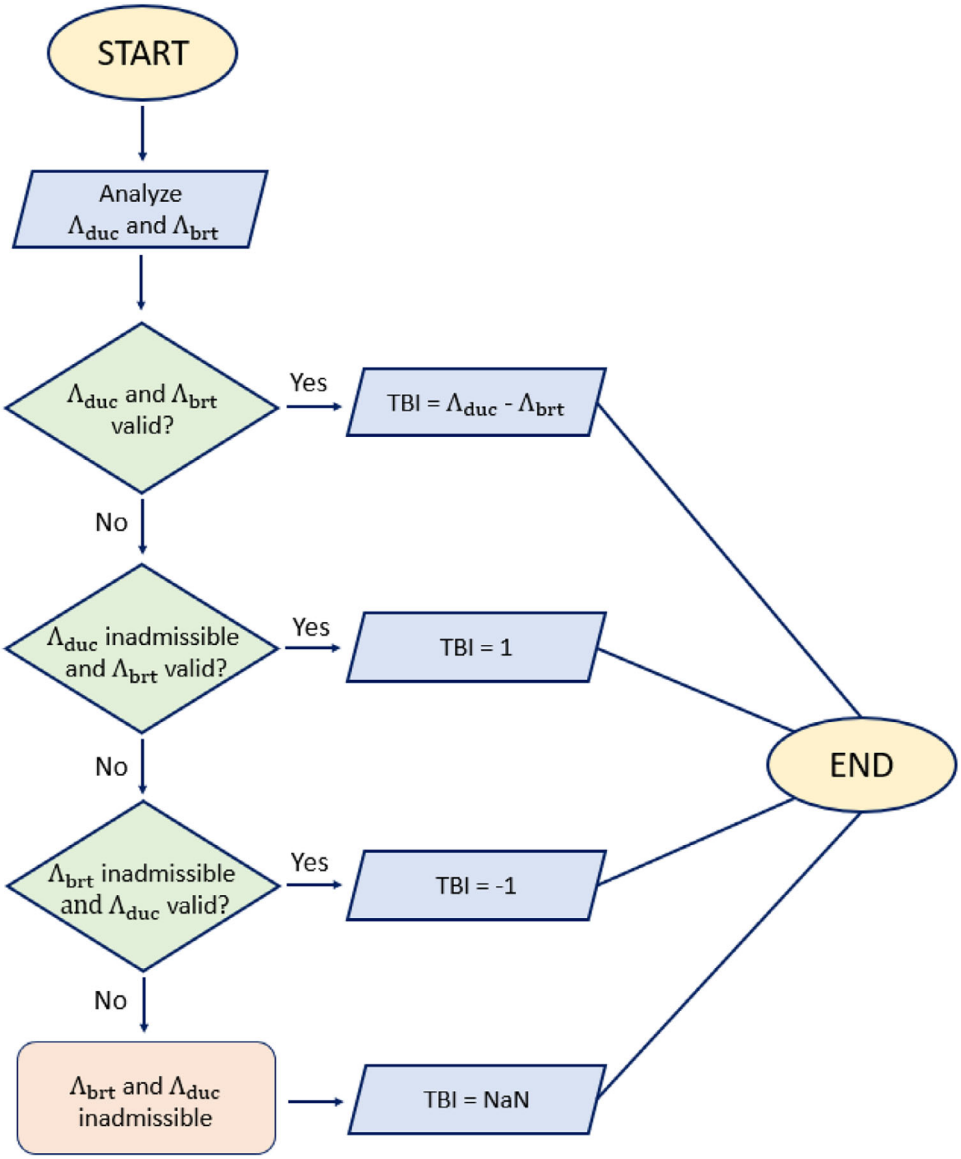


**FIGURE 5** | Flow chart for the computation of TBI. Λ is considered admissible if in the range 0–1, otherwise it is inadmissible.

on an experimental campaign. Further details on this matter will be described in Section 4.

The approach proposed by Bažant et al. [52] is based on the results of direct shear tests at the constant crack opening on concrete (reported in [68]). Since a particular feature of compression splitting cracks is that their opening displacement is null, laboratory tests conducted at null crack opening should be considered. The shear stiffness $k_s$ of the crack could be computed as the slope of the linear part of the stress-displacements curve, provided by the shear test, that is, $(\tau/\Delta)_0$. Then, recalling that $\lambda$ is defined as:

$$\lambda = \frac{G_i}{k_s} \tag{40}$$

this result could be used to compute $\lambda$ as:

$$\lambda = \frac{G_i}{(\tau/\Delta)_0} \tag{41}$$

However, Bažant et al. [52] noticed that no experimental results seemed to be available for the null crack width condition, so an extrapolation of the results related to crack widths of 0.25 and 0.5 mm was performed to estimate $(\tau/\Delta)_0$. Bažant et al. [52] did not report directly the obtained value of $(\tau/\Delta)_0$, but asserted that, considering a shear modulus $G_i = 11.25$ GPa, the value $\lambda \approx 0.1$ m can be obtained. This means that $(\tau/\Delta)_0 \approx 112.5$ GPa/m. Using this method means that the number of independent parameters on which TBI depends is reduced by 1. Nonetheless, it was decided to leave $\lambda$ in evidence in the expression of TBI to allow its evaluation using any other more accurate methods, if available.

### 3.2 | Application of TBI to a Real Case

In order to illustrate the step-by-step procedure for calculating TBI and its effectiveness, a real case study of brittle failure around a deep excavation is here considered. Specifically, the spalling failure of one of the Jinping II tunnels is examined, as it is well documented by Qiu et al. [53] and Gong et al. [69].

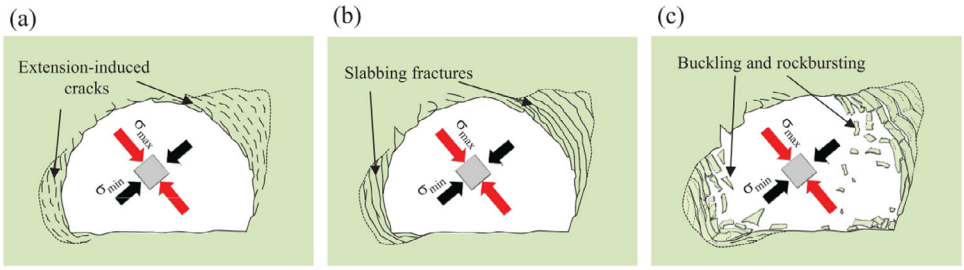


**FIGURE 6** | Slabbing, buckling, and rockburst a Jinping II tunnel: (a) development of extension fractures caused by stress concentration; (b) occurrence of rock slabbing; and (c) damage from rockburst and expulsion of rock blocks triggered by slab buckling [53].

**TABLE 5** | Values of the 9 input parameters used for the application of TBI to the case study of the vertical rise of the Garpenberg mine.

| Parameter | Value | Source |
|---|---|---|
| $\sigma_{y\infty}$ | 57 MPa | IFL |
| $k$ | 0.5 | IFL |
| $\nu$ | 0.26 | IFL |
| $E$ | 50.7 GPa | IFL |
| $A$ | 0.45 MPa | Calculated |
| $B$ | 0.56 | Calculated |
| $G_i$ | 21.1 GPa | Calculated |
| $\mathcal{G}_f$ | $7.1 \cdot 10^{-6}$ MPa· m | Calculated |
| $\lambda$ | 2.28 | IFL |

*Note:* "IFL" stands for "information found in the literature"; in this case, the information comes from Edelbro [70] and Edelbro [71].

The Jinping II tunnels, located in the southwestern region of China, are an integral part of the Jinping II Hydropower Station, one of China's largest hydropower projects. They traverse through diverse geological formations, primarily composed of competent rocks such as granite, gneiss, and marble, and operate under high geostatic stresses. Consistently with the brittle failure models presented above, the researchers observed that, following the excavation of these tunnels, widespread extension fractures formed as a result of the unloading process and the consequent high circumferential stresses. These fractures emerged in parallel sets in the stress concentration zone surrounding the excavation, leading the originally intact rock mass to become fragmented into multiple rock slabs, which gave rise to the phenomenon of "slabbing" or "spalling" schematized in Figure 6.

The considered excavation is a circular tunnel with a diameter of 6.2 m, excavated in marble and subjected to in-plane geostatic stresses of about 53 and 31 MPa.

Table 5 reports the assumed values for the 9 input parameters of TBI for the Jinping II tunnel, by which the values $\Lambda_{duc} = 1.14$ and $\Lambda_{brt} = 0.12$ can be obtained. In this regard, it should be noted that:

- The value of $\lambda$ was found in the literature. Specifically, it was calculated by Qiu et al. [53] using the approach they proposed, which is based on the analysis of real splitting fracture surfaces.
- $G_i$ was computed using Equation (37).
- $A$ and $B$ were calculated using Equation (21) as functions of the rock mass unconfined compressive strength $\sigma_{c,rm} = 26.3$ MPa and uniaxial tensile strength $\sigma_{t,rm} = 0.4$ MPa. These values were estimated based on information from the literature.
- $\mathcal{G}_f$ was calculated using Equation (38), with $k_{IC} = 0.62$ MPa · $m^{1/2}$ estimated using Equation (39) ($\sigma_{t,i} = 4.27$ MPa, as found in the literature).

The values $\Lambda_{duc}$ and $\Lambda_{brt}$ obtained indicate that, in this case, $\Lambda_{duc}$ assumes a value with no physical meaning (inadmissible), as it is greater than 1, while $\Lambda_{brt}$ assumes an admissible value. According to the computation algorithm described in Section 3 and shown in Figure 5, the final result TBI = 1 is obtained, which corresponds to the maximum prevalence of the brittle failure mechanism over the ductile one. This result is consistent with the observed failure mode (brittle, in the form of spalling) and indicates that brittle failure is likely to occur during the excavation of the tunnel, while ductile failure is unlikely. This information, if obtained in the early stages of a deep tunnel design to forecast purposes, could be useful to choose the most appropriate excavation techniques and methods, as well as the support systems.

Certainly, it is important to notice that a validation of the proposed approach is essential before using TBI as a design tool. This activity, which will be highlighted in Section 4 as one of the most interesting future developments of the research described here, is actually an ongoing work and is being based on a dataset of real case studies of brittle and ductile failure around deep tunnels.

## 4 | Discussion

This section presents a discussion on the functioning and application conditions of TBI, with a particular focus on some specific features.

The analytical model used, the rock mass in which the tunnel is excavated is considered as a continuous, linear-elastic, isotropic medium, subjected to an anisotropic original stress state, described by the stress tensor $\boldsymbol{\sigma}$, which corresponds to oedometric conditions, as it is characterized by isotropic natural stresses within the horizontal plane ($xz$, with reference to Figure 2). The vertical geostatic stress in the cross-section plane, $\sigma_{y\infty}$, is assumed as the maximum principal geostatic stress (hence, $0 \leq k \leq 1$)

and all the horizontal geostatic stresses are principal stresses. Moreover, the tunnel axis is assumed to be perpendicular to the maximum principal stress, that is, horizontal. The assumption of a vertical maximum principal geostatic stress was dictated by reasons of simplicity in the formulation. However, such an assumption does not imply that the validity and applicability of the calculation results are limited to cases where the maximum geostatic stress is vertical. In fact, any rotation of the principal stresses in the cross-sectional plane of the tunnel can be considered without loss of generality of the solution. To achieve this, it is sufficient to assign to $\sigma_{y\infty}$ the value of the actual maximum in situ geostatic stress, regardless of its orientation, and calculate $k$ based on the geostatic stress orthogonal to the first one. This approach allows to consider in the calculations a stress ratio $k$ always between 0 and 1, a requirement necessary for the use of the expressions of $\Lambda_{duc}$ and $\Lambda_{brt}$, and a reference system $xy$ (indicated in Figure 2) with axes not necessarily horizontal and vertical but oriented according to the actual geostatic stresses ($y$ axis parallel to the maximum principal geostatic stress). However, it is reiterated that this characteristic does not limit the applicability of TBI, as the only effects of the actual orientation of the geostatic stresses in situ are the position of the points called "crown" and "sidewall" (not necessarily placed on the vertical and horizontal axes but always associated with the values $\theta = 0°$ and $\theta = 90°$, respectively) and the position of the fracture zones assumed in the brittle failure model. On the contrary, in the analytical calculations, it was not possible to eliminate the requirement that the tunnel axis be parallel to a principal direction and orthogonal to the maximum principal geostatic stress, that is, horizontal. Consequently, this condition constitutes a prerequisite for the applicability of the model and a limitation to the validity of its predictions.

The indication of the prevalence of one failure mode over the other is grounded on physically based mechanical models, but the prediction of failure in absolute terms is not as accurate as that provided by more sophisticated analyses such as numerical simulations. In particular, in the cases where the TBI index was not applicable (i.e., TBI = NaN), neither of the two considered damage models anticipated rock failure under the analyzed conditions. It is believed that this occurrence is not necessarily related to conditions in which failure cannot actually occur but could rather be attributed to inaccuracies in parameter estimates or the limitations of the analytical models used here. Other failure processes could, in fact, occur, for example, related to the discontinuous nature of the rock mass (i.e., some specific geostructural condition could lead to failure, for example, the presence of joints forming unstable rock blocks). In such cases, it is essential to consider the probability of occurrence of failure phenomena that are not encompassed by the presented mechanical damage models, for which alternative stability analysis methods become necessary.

Finally, it is important to notice that the method does not consider the transition between brittle and ductile behavior. Rather, it is assumed that both failure modes may occur under a given set of boundary conditions, and the two mechanisms are analyzed separately. The method provides the two critical values of the excavation parameter $\Lambda$, each one triggering one of the two failure mechanisms. By analyzing the two failure onset conditions, the method solely quantifies the outcome of the competition between the two mechanisms in terms of the prevalence of one over the other. Finally, this information is used to estimate the propensity of the rock mass for brittle failure, which is considered the more hazardous failure mode. Ultimately, the method discriminates between the two phenomena, identifying which one occurs first during excavation.

Specifically, the model does not analyze the absolute mechanical behavior of a rock mass, but rather assesses its response to the excavation process. Under certain boundary conditions, the propensity of the rock mass toward brittle failure is not absolute, as it can exhibit both failure mechanisms. In these intermediate cases, in which TBI assumes values between 0 and 1 (excluding the extremes), the rock mass behavior can be considered quasi-brittle.

As can be observed, the method proposed in this paper does not consider the influence of tunnel size on the rock mass's propensity for brittle failure. Indeed, the tunnel radius ($R$) is not one of the input parameters for calculating TBI. This characteristic falls within the method's approximations, which, being analytical in nature, inherently involves certain simplifications. The contribution of $R$ is lost due to simplifications in the analytical solutions of the two models describing the two damage mechanisms in rock (ductile and brittle). In the case of the ductile failure model, $R$ is eliminated when focusing the search for failure conditions on the tunnel boundary (where $\rho = 1$). Conversely, in the brittle failure model, the contribution of $R$ is disregarded when assuming that tunnels can be considered large cavities, enabling an approximate solution for Equation (34) (a fifth-degree equation). In this case, the simplification aligns with the approach by Qiu et al. [53], as the original model by Bažant et al. [52] allowed applications to both small holes (such as boreholes) and large cavities (such as underground caverns).

## 5 | Conclusions

The possibility to predict the failure mode of the rock mass when designing deep underground constructions is of paramount importance to face sudden, high energy, dangerous phenomena like rockburst and spalling. This paper presents a novel methodological approach to forecast the failure mode of the rock mass around a deep tunnel, during the excavation phase. Consistent mechanical models are used to interpret both the plastic and the brittle failure, modeling the progressive stress release due to the excavation process by the well-known progressive reduction of the fictitious pressure inside the cavity, from the initial geostatic value to zero. The application of these models leads to the definition of a new, physically based brittleness index for deep tunnels.

Differently from the classic analytical solutions available in the literature for plastic failure around a tunnel, here a general natural stress state is considered, overcoming the isotropic stress assumption ($k = 1$). Moreover, a 3D failure criterion is considered for the rock mass. On the other hand, brittle failure is interpreted by expanding the model proposed by Bažant et al. [52] to account for the progressive stress relief induced by the excavation.

The two failure mechanisms, brittle and ductile, are made to compete with each other, and that associated with the lowest

stress reduction is assumed to be the most likely one. A new brittleness index based on 9 parameters, called TBI, is calculated to identify the dominant failure mode of the rock mass. The effectiveness and the application of TBI are shown with reference to a real case study of brittle (spalling) failure around a deep circular excavation.

The proposed TBI has a modular logic structure which allows to adopt a possible different, more accurate model to interpret the brittle response of the rock mass to the stress release, without changing the procedure for the determination of TBI. Hence, the proposed method lends itself well to future improvements or extensions. For these reasons, TBI appears as a promising and useful tool for engineers dealing with deep tunnels projects, in which spalling and/or rockburst may occur.

Certainly, it is important to note that the definition of TBI is based on the development and use of analytical and, therefore, simplified rock damage models. Such models do not provide an exact description of rock behavior but rather an approximation. For this reason, TBI should be considered a preliminary tool, but a rational one, for predicting the most likely failure mode of the rock mass in the early stages of designing a deep tunnel.

Improvements and future developments of the proposed methodology, based on the results presented here, can be highlighted, and some of them are the subject of currently ongoing research.

First, a robust validation of the approach proposed is recognized as crucial for the use of TBI as a predictive design tool. This activity should be performed considering a large dataset of case studies of brittle and ductile failure around deep excavations, documented in the literature, also if non-negligible difficulties in reliably quantifying the values of the 9 parameters required for the calculation of TBI are expected when dealing with past events.

Moreover, it would be useful to carry out a sensitivity analysis of the brittleness index, in order to determine the influence of each input parameter. The result of this analysis would allow one to assign a weight to each independent parameter and indicate, to the practitioner intending to use the index, which parameters should be estimated with greater accuracy to improve the reliability of the result. Furthermore, these weights could be combined with a second set of weights assigned to each of the parameters values, depending on the confidence with which they have been determined.

Finally, it would be important to define a simple, accurate, and repeatable procedure for quantifying the shear stiffness of splitting fractures, $k_s$, which is the fundamental ingredient for estimating the critical parameter $\lambda$. In fact, based on the results of preliminary sensitivity analyses, $\lambda$ appears as one of the most important input parameters. This activity, which could help to reduce the uncertainty associated with $\lambda$, is already planned as part of the continuation of the research presented here and will likely involve performing ultrasonic measurements on induced splitting fractures in specimens of different lithotypes. The results of the experimentation could allow the creation of a dataset of $\lambda$ (or $k_s$) values for different lithotypes, beneficial for an easy application of TBI to a tunnel in the design phase.

### Author Contributions

Conceptualization: Lorenzo Milan, Mauro Borri-Brunetto, and Monica Barbero. Methodology: Lorenzo Milan, Mauro Borri-Brunetto, and Monica Barbero. Software: Lorenzo Milan and Mauro Borri-Brunetto. Validation: Mauro Borri-Brunetto and Monica Barbero. Formal analysis: Lorenzo Milan. Investigation: Lorenzo Milan. Data curation: Lorenzo Milan. Writing–original draft preparation: Lorenzo Milan. Writing–review and editing: Lorenzo Milan, Mauro Borri-Brunetto, and Monica Barbero. Supervision: Mauro Borri-Brunetto and Monica Barbero. Project administration: Lorenzo Milan.

### Acknowledgments

The authors have no relevant financial or non-financial interests to disclose.

### Conflicts of Interest

The authors declare no potential conflicts of interest.

### Data Availability Statement

Data supporting reported results can be obtained upon request to the author.

### Endnotes

[1]The routine was integrated in an executable standalone app that can be found in the public GitHub repository https://github.com/LorenzoMilan/TBI-Computation_App

### References

1. M. Cai, "Principles of Rock Support in Burst-Prone Ground," *Tunnelling and Underground Space Technology* 36, no. 06 (2013): 46–56.

2. F. Gong, Y.-l. Wang, and S. Luo, "Rockburst Proneness Criteria for Rock Materials: Review and New Insights," *Journal of Central South University* 27, no. 10 (2020): 2793–2821.

3. M. Askaripour, A. Saeidi, A. Rouleau, and P. Mercier-Langevin, "Rockburst in Underground Excavations: A Review of Mechanism, Classification, and Prediction Methods," *Underground Space* 7, no. 4 (August 2022): 577–607.

4. I. Benamar, "Etude des Effets Différés dans les Tunnels Profonds" (PhD thesis, Ecole Nationale des Ponts et Chaussées, 1996).

5. W. C. Ferrão, "Estudo de túneis superficiais: influência na convergência e no perfil de assentamento" (PhD 526 thesis, Universidade Federal Do Rio Grande Do Sul - Escola De Engenharia, 2018).

6. M. Diederichs, "The 2003 Canadian Geotechnical Colloquium: Mechanistic Interpretation and Practical Application of Damage and Spalling Prediction Criteria for Deep Tunneling," *Canadian Geotechnical Journal* 44, no. 09 (2007): 1082–1116.

7. M. Cai and E. Brown, "Challenges in the Mining and Utilization of Deep Mineral Resources," *Engineering* 3, no. 08 (2017): 432–433.

8. P. Kaiser and M. Cai, *Rockburst Support Reference Book–Volume I: Rockburst Phenomenon and Support Characteristics* (Geomechanics Research Centre / MIRARCO, 2018). ISBN 978-0-88667-096-2.

9. R. Q. Huang, X. N. Wang, and L. S. Chan, "Triaxial Unloading Test of Rocks and Its Implication for Rock Burst," *Bulletin of Engineering Geology and the Environment* 60, no. 1 (April 2001): 37–41.

10. F. Amann, E. A. Button, K. F. Evans, V. S. Gischig, and M. Blümel, "Experimental Study of the Brittle Behavior of Clay Shale in Rapid Unconfined Compression," *Rock Mechanics and Rock Engineering* 44, no. 4 (May 2011): 415–430.

11. L. Sousa, "Report for the State Administration of Foreign Experts Affairs," Technical report, State Key Laboratory for GeoMechanics and Deep Underground Engineering of China (University of Porto (Portugal), Porto, 02 2012).

12. M. He, L. R. e Sousa, T. Miranda, and G. Zhu, "Rockburst Laboratory Tests Database—Application of Data Mining Techniques Application of Data Mining Techniques," *Engineering Geology* 185 (February 2015): 116–130.

13. F.-Q. Gong, Y. Luo, X.-B. Li, X.-F. Si, and M. Tao, "Experimental Simulation Investigation on Rockburst Induced By Spalling Failure in Deep Circular Tunnels," *Tunnelling and Underground Space Technology* 81 (November 2018): 413–427.

14. Y. Chen, J. Zhang, J. Zhang, B. Xu, L. Zhang, and W. Li, "Rockburst Precursors and the Dynamic Failure Mechanism of the Deep Tunnel: A Review," *Energies* 14, no. 22 (November 2021): 7548.

15. M. He, T. Cheng, Y. Qiao, and H. Li, "A Review of Rockburst: Experiments, Theories, and Simulations," *Journal of Rock Mechanics and Geotechnical Engineering* 15, no. 5 (2022): 1312–1353.

16. W. Blake, "Rockburst Mechanics," *Colorado School of Mines* 67, no. 1 (1972): 1–64.

17. N. G. W. Cook, "Seismicity Associated With Mining," *Engineering Geology* 10, no. 2-4 (December 1976): 99–122.

18. P. K. Kaiser, D. R. McCreath, and D. D. Tannant, *Canadian Rockburst Support Handbook* (Geomechanics Research Center, 1996).

19. W. D. Ortlepp, *Rock Fracture and Rockbursts: An Illustrative Study*, Vol. 9 (South African Institute of Mining and Metallurgy, 1997).

20. E. Hoek, P. K. Kaiser, and W. F. Bawden, *Support of Underground Excavations in Hard Rock* (CRC Press, 2000).

21. A. Mazaira and P. Konicek, "Intense Rockburst Impacts in Deep Underground Construction and Their Prevention," *Canadian Geotechnical Journal* 52, no. 10 (October 2015): 1426–1439.

22. T. Li, C. Ma, M. Zhu, L. Meng, and G. Chen, "Geomechanical Types and Mechanical Analyses of Rockbursts," *Engineering Geology* 222 (May 2017): 72–83.

23. X. Liu, S. Zhan, Y. Zhang, X. Wang, Z. Liang, and B. Tian, "The Mechanical and Fracturing of Rockburst in Tunnel and Its Acoustic Emission Characteristics," *Shock and Vibration* 2018 (June 2018): 1–11.

24. Z. Liang, X. Liu, Y. Zhang, and C. Tang, "Analysis of Precursors Prior to Rock Burst in Granite Tunnel Using Acoustic Emission and Far Infrared Monitoring," *Mathematical Problems in Engineering* 2013 (2013): 1–10.

25. A. M. Naji, M. Z. Emad, H. Rehman, and H. Yoo, "Geological and Geomechanical Heterogeneity in Deep Hydropower Tunnels: A Rock Burst Failure Case Study," *Tunnelling and Underground Space Technology* 84 (February 2019): 507–521.

26. W. D. Ortlepp and T. R. Stacey, "Rockburst Mechanisms in Tunnels and Shafts," *Tunnelling and Underground Space Technology* 9, no. 1 (January 1994): 59–65.

27. Z. Weishen, L. Yong, L. Shucai, W. Shugang, and Z. Qianbing, "Quasi-Three-Dimensional Physical Model Tests on a Cavern Complex Under High In-Situ Stresses," *International Journal of Rock Mechanics and Mining Sciences* 48, no. 2 (February 2011): 199–209.

28. S. Li, X.-T. Feng, Z. Li, B. Chen, C. Zhang, and H. Zhou, "In Situ Monitoring of Rockburst Nucleation and Evolution in the Deeply Buried Tunnels of Jinping II Hydropower Station," *Engineering Geology* 137-138 (June 2012): 85–96.

29. S. Zhai, G. Su, S. Yin, B. Zhao, and L. Yan, "Rockburst Characteristics of Several Hard Brittle Rocks: A True Triaxial Experimental Study," *Journal of Rock Mechanics and Geotechnical Engineering* 12, no. 2 (April 2020): 279–296.

30. R. G. Khanlari, "Analysis of Rock Burst in Critical Section of Second Part of Karaj–Tehran Water Supply Tunnel," in *ISGSR 2011: Proceedings of the 3rd International Symposium on Geotechnical Safety and Risk* (Karlsruhe, Germany: Bundesanstalt für Wasserbau, 2011).

31. M. Ahmad, J.-L. Hu, M. Hadzima-Nyarko, et al., "Rockburst Hazard Prediction in Underground Projects Using Two Intelligent Classification Techniques: A Comparative Study," *Symmetry* 13, no. 4 (April 2021): 632.

32. L. N. Germanovich and A. V. Dyskin, "Fracture Mechanisms and Instability of Openings in Compression," *International Journal of Rock Mechanics and Mining Sciences* 37, no. 1-2 (January 2000): 263–284.

33. F. Meng, L. N. Y. Wong, and H. Zhou, "Rock Brittleness Indices and Their Applications to Different Fields of Rock Engineering: A Review," *Journal of Rock Mechanics and Geotechnical Engineering* 13, no. 1 (February 2021): 221–247.

34. J. Zhou, X. Li, and H. Mitri, "Evaluation Method of Rockburst: State-of-the-Art Literature Review," *Tunnelling and Underground Space Technology* 81 (November 2018): 632–659.

35. C. S. Qiao and Z. Y. Tian, "Study of the Possibility of Rockburst in Dong-Gua-Shan Copper Mine ua-Shan Copper Mine," *Chinese Journal of Rock Mechanics and Engineering* 17, no. 1998 (1998): 917–921.

36. J.-A. Wang and H. D. Park, "Comprehensive Prediction of Rockburst Based on Analysis of Strain Energy in Rocks," *Tunnelling and Underground Space Technology* 16, no. 1 (January 2001): 49–57.

37. E. T. Brown and E. Hoek, *Underground Excavations in Rock* (CRC Press, 1980).

38. I. A. Turchaninov, G. A. Markov, M. V. Gzovsky, et al., "State of Stress in the Upper Part of the Earth's Crust Based on Direct Measurements in Mines and on Tectonophysical and Seismological Studies," *Physics of the Earth and Planetary Interiors* 6, no. 4 (January 1972): 229–234.

39. B. Khadivi, H. Masoumi, A. Heidarpour, Q. Zhang, and J. Zhao, "Assessing the Fracturing Process of Rocks Based on Burst–Brittleness Ratio (BBR) Governed by Point Load Testing," *Rock Mechanics and Rock Engineering* 56, no. 11 (August 2023): 8167–8189, https://doi.org/10.1007/s00603-023-03491-0.

40. H. Masoumi, S. Saydam, and P. C. Hagan, "Unified Size-Effect Law for Intact Rock," *International Journal of Geomechanics* 16, no. 2 (April 2016), https://doi.org/10.1061/(asce)gm.1943-5622.0000543.

41. H. Farhadian, "A New Empirical Chart for Rockburst Analysis in Tunnelling: Tunnel Rockburst Classification (TRC)," *International Journal of Mining Science and Technology* 31, no. 4 (July 2021): 603–610.

42. B. Neyman, Z. Szecowka, and W. Zuberek, "Effective Methods for Fighting Rock Burst in Polish Collieries," in *Proceedings of the 5th International Strata Control Conference* (South African Institute of Mining and Metallurgy, 1995), 1–9.

43. M. Panet, *Calcul des Tunnels par la Méthode Convergence-Confinement* (Presses de l'Ecole Nationale des Ponts et Chaussées, 1995). ISBN 9782859782306.

44. C. Carranza-Torres and C. Fairhurst, "Application of the Convergence-Confinement Method of Tunnel Design to Rock Masses that Satisfy the Hoek–Brown Failure Criterion," *Tunnelling and Underground Space Technology* 15, no. 2 (2000): 187–213.

45. E. Alonso, L. Alejano, F. Varas, G. Fdez-Manin, and C. Carranza-Torres, "Ground Response Curves for Rock Masses Exhibiting Strain-Softening Behavior," *International Journal for Numerical and Analytical Methods in Geomechanics* 27, no. 13 (November 2003): 1153–1185.

46. C. Carranza-Torres, "Elasto-Plastic Solution of Tunnel Problems Using the Generalized Form of the Hoek–Brown Failure Criterion," *International Journal of Rock Mechanics and Mining Sciences* 41 (2004): 629–639.

47. L. R. Alejano, A. Rodriguez-Dono, E. Alonso, and G. Fdez-Manín, "Ground Reaction Curves for Tunnels Excavated in Different Quality Rock Masses Showing Several Types of Post-Failure Behaviour," *Tunnelling and Underground Space Technology* 24, no. 6 (November 2009): 689–705.

48. P. Oreste, "The Convergence-Confinement Method: Roles and Limits in Modern Geomechanical Tunnel Design," *American Journal of Applied Sciences* 6, no. 4 (April 2009): 757–771.

49. N. Vlachopoulos and M. S. Diederichs, "Improved Longitudinal Displacement Profiles for Convergence Confinement Analysis of Deep Tunnels," *Rock Mechanics and Rock Engineering* 42, no. 2 (April 2009): 131–146.

50. J. González-Cao, F. Varas, F. Bastante, and L. Alejano, "Ground Reaction Curves for Circular Excavations in Non-Homogeneous, Axisymmetric Strain-Softening Rock Masses," *Journal of Rock Mechanics and Geotechnical Engineering* 5, no. 6 (2013): 431–442.

51. S. Deng, Y. Zheng, L. Feng, L. Van Tuan, C. Yue, and Z. Wu, "Analysis of Plastic Zones in Surrounding Rocks Around a Circular Tunnel Considering the Effect of Intermediate Principal Stress and Heterogeneity," *MATEC Web of Conferences* 275 (January 2019): 03007.

52. Z. P. Bažant, F.-B. Lin, and H. Lippmann, "Fracture Energy Release and Size Effect in Borehole Breakout," *International Journal for Numerical and Analytical Methods in Geomechanics* 17, no. 1 (January 1993): 1–14.

53. S. Qiu, X. Feng, C. Zhang, and T. Xiang, "Estimation of Rockburst Wall-Rock Velocity Invoked by Slab Flexure Sources in Deep Tunnels," *Canadian Geotechnical Journal* 51, no. 5 (May 2014): 520–539.

54. C. D. Martin, "Seventeenth Canadian Geotechnical Colloquium: The Effect of Cohesion Loss and Stress Path on Brittle Rock Strength," *Canadian Geotechnical Journal* 34, no. 5 (October 1997): 698–725.

55. C. D. Martin, R. S. Read, and J. B. Martino, "Observations of Brittle Failure Around a Circular Test Tunnel," *International Journal of Rock Mechanics and Mining Sciences* 34, no. 7 (October 1997): 1065–1073.

56. S. Timoshenko and J. N. Goodier, *Theory of Elasticity*, Engineering societies Monographs (McGraw-Hill, 1951).

57. J. C. Jaeger, N. G. W. Cook, and R. Zimmerman, *Fundamentals of Rock Mechanics* (Blackwell Publishing, 2007).

58. G. E. Exadaktylos and C. E. Tsoutrelis, "Pillar Failure by Axial Splitting in Brittle Rocks," *International Journal of Rock Mechanics and Mining Sciences* 32, no. 6 (September 1995): 551–562.

59. B. Singh, M. N. Viladkar, N. K. Samadhiya, and Sandeep, "A Semi-Empirical Method for the Design of Support Systems in Underground Openings," *Tunnelling and Underground Space Technology* 10, no. 3 (July 1995): 375–383.

60. M. Stavropoulou, G. Exadaktylos, and G. Saratsis, "A Combined Three-Dimensional Geological-Geostatistical-Numerical Model of Underground Excavations in Rock," *Rock Mechanics and Rock Engineering* 40, no. 3 (January 2007): 213–243.

61. T. Mura, *Micromechanics of Defects in Solids* (Martinus Nijhoff Publishers, 1987). ISBN 9789024732562.

62. E. Grimstad and N. Barton, "Updating the Q-System for NMT," *Proceedings of the International Symposium on Sprayed Concrete* 7, no. 2 (January 1993): 46–66.

63. N. Barton, "Barton, 1996. Estimating rock mass deformation modulus for excavation disturbed zone studies," in *Proceedings of the Excavation Disturbed Zone Workshop "Designing the Excavation Disturbed Zone for a Nuclear Repository in Hard Rock"* (1996), 1–12.

64. E. Hoek, C. Carranza-Torres, B. Corkum, E. Hoek, and C. Carranza-Torres, "Hoek–Brown Failure Criterion—2002 Edition," in *Proceedings of the 5th North American Rock Mechanics Symposium and the 17th Tunnelling Association of Canada Conference: NARMS-TAC 2002, Toronto, 7-10 July 2002* (2002), 267–273.

65. E. Hoek and M. Diederichs, "Empirical Estimation of Rock Mass Modulus," *International Journal of Rock Mechanics and Mining Sciences* 43, no. 2 (February 2006): 203–215.

66. Z. X. Zhang, "An Empirical Relation Between Mode I Fracture Toughness and the Tensile Strength of Rock Fracture Toughness and the Tensile Strength of Rock," *International Journal of Rock Mechanics and Mining Sciences* 39, no. 3 (April 2002): 401–406.

67. B. N. Whittaker, R. N. Singh, and G. Sun, *Rock Fracture Mechanics: Principles, Design, and Applications* (Elsevier, 1992).

68. Z. P. Bažant and P. G. Gambarova, "Rough Cracks in Reinforced Concrete," *ASCE Journal of the Structural Division* 106 (April 1980): 819–842.

69. Q. M. Gong, L. J. Yin, S. Y. Wu, J. Zhao, and Y. Ting, "Rock Burst and Slabbing Failure and Its Influence on TBM Excavation at Headrace Tunnels in Jinping II Hydropower Station," *Engineering Geology* 124 (2012): 98–108.

70. C. Edelbro, "*Strength of Hard Rock Masses: A Case study*," Technical Report 2006: 13 (LuleåUniversity of Technology, Mining and Geotechnical Engineering, 2006).

71. C. Edelbro, "Numerical Modelling of Observed Fallouts in Hard Rock Masses Using an Instantaneous Cohesion-Softening Friction-Hardening Model," *Tunnelling and Underground Space Technology* 24, no. 4 (2009): 398–409.

72. Wolfram Research, Inc., "Mathematica, Version 14.0" (Champaign, IL, 2024).

73. J. R. Barber, "Linear Elastostatics," in *Continuum Mechanics*, Vol. I, ed. J. Merodio and G. Saccomandi (EOLSS Publ., 2011).

## Appendix A

In the following some calculations and complete mathematical expressions of the quantities mentioned in the text are reported. All the computations described in this paper were performed using the software Mathematica [72].

### Solution of Case 2 (Stress Induced by Unloading)

The approach followed for the determination of the stresses induced by the components of the original stress state depending on $\theta$ is described below.

The differential equations of equilibrium in polar coordinates are (e.g., [56][p. 56]):

$$\begin{aligned} \frac{\partial \sigma_r}{\partial r} + \frac{1}{r}\frac{\partial \tau_{r\theta}}{\partial \theta} + \frac{\sigma_r - \sigma_\theta}{r} = 0 \\ \frac{1}{r}\frac{\partial \sigma_\theta}{\partial \theta} + \frac{\partial \tau_{r\theta}}{\partial r} + \frac{2\tau_{r\theta}}{r} = 0 \end{aligned} \tag{A1}$$

These equations are satisfied by setting:

$$\begin{aligned} \sigma_r^{(2)} &= \frac{1}{r}\frac{\partial \phi}{\partial r} + \frac{1}{r^2}\frac{\partial^2 \phi}{\partial \theta^2} \\ \sigma_\theta^{(2)} &= \frac{\partial^2 \phi}{\partial r^2} \\ \tau_{r\theta}^{(2)} &= \frac{1}{r^2}\frac{\partial \phi}{\partial \theta} - \frac{1}{r}\frac{\partial^2 \phi}{\partial r \partial \theta} = -\frac{\partial}{\partial r}\left(\frac{1}{r}\frac{\partial \phi}{\partial \theta}\right) \end{aligned} \tag{A2}$$

where $\phi(r, \theta)$ is the Airy stress function. Hence, the compatibility equation of the plate acquires the form:

$$\left(\frac{\partial^2}{\partial r^2} + \frac{1}{r}\frac{\partial}{\partial r} + \frac{1}{r^2}\frac{\partial^2}{\partial \theta^2}\right)\left(\frac{\partial^2 \phi}{\partial r^2} + \frac{1}{r}\frac{\partial \phi}{\partial r} + \frac{1}{r^2}\frac{\partial^2 \phi}{\partial \theta^2}\right) = 0 \tag{A3}$$

As shown by [56], the symmetry of the problem allows one to define $\phi(r, \theta)$ as the product between two functions of one variable each, of the form:

$$\phi(r, \theta) = f(r)\cos(2\theta) \tag{A4}$$

Substituting Equation (A4) in Equation (A3), we obtain an ordinary differential equation, whose solution $f(r)$ depends on four constants,

$(A, B, C, D,)$ to be determined according to the boundary conditions:

$$f(r) = Ar^2 + Br^4 + C\frac{1}{r^2} + D$$
$$\phi(r,\theta) = \left(Ar^2 + Br^4 + C\frac{1}{r^2} + D\right)\cos(2\theta) \tag{A5}$$

Using Equation (A5), the stress components provided by Equation (A2) can be written as:

$$\sigma_r = -\left(2A + \frac{6C}{r^4} + \frac{4D}{r^2}\right)\cos(2\theta)$$
$$\sigma_\theta = \left(2A + 12Br^2 + \frac{6C}{r^4}\right)\cos(2\theta) \tag{A6}$$
$$\tau_{r\theta} = \left(2A + 6Br^2 - \frac{6C}{r^4} - \frac{2D}{r^2}\right)\sin(2\theta)$$

The four constants were computed using the following four boundary conditions:

- For $r = R$:

$$\sigma_r = \sigma_{r,0}^{(2)} = \frac{\sigma_{x\infty} - \sigma_{y\infty}}{2}\cos(2\theta)$$
$$\tau_{r\theta} = \tau_{r\theta,0}^{(2)} = \frac{\sigma_{y\infty} - \sigma_{x\infty}}{2}\sin(2\theta) \tag{A7}$$

- For $r = b$:

$$\sigma_r = (1-\Lambda)\sigma_{r,0}^{(2)} = (1-\Lambda)\frac{\sigma_{x\infty} - \sigma_{y\infty}}{2}\cos(2\theta)$$
$$\tau_{r\theta} = (1-\Lambda)\tau_{r\theta,0}^{(2)} = (1-\Lambda)\frac{\sigma_{y\infty} - \sigma_{x\infty}}{2}\sin(2\theta) \tag{A8}$$

The final values of the constants were obtained calculating the limits for $b \to \infty$:

$$A = \frac{\sigma_{y\infty} - \sigma_{x\infty}}{2}$$
$$B = 0$$
$$C = \frac{\sigma_{y\infty} - \sigma_{x\infty}}{2}R^4\Lambda \tag{A9}$$
$$D = \frac{\sigma_{y\infty} - \sigma_{x\infty}}{2}R^2\Lambda$$

Hence, the stresses induced induced by case 2 were computed setting $\sigma_{x,\infty} = k\sigma_{y,\infty}$ and substituting Equation (A9) in Equation (A6) with $r = \rho R$:

$$\frac{\sigma_r^{(2)}}{\sigma_{y\infty}} = \frac{(k-1)\left[\rho^4 + \Lambda\left(3 - 4\rho^2\right)\right]}{2\rho^4}\cos(2\theta)$$
$$\frac{\sigma_\theta^{(2)}}{\sigma_{y\infty}} = \frac{-(k-1)(3\Lambda + \rho^4)}{2\rho^4}\cos(2\theta) \tag{A10}$$
$$\frac{\tau_{r\theta}^{(2)}}{\sigma_{y\infty}} = \frac{-(k-1)[\rho^4 + \Lambda(2\rho^2 - 3)]}{2\rho^4}\sin(2\theta)$$

## Appendix B

### Expression of the Drucker–Prager Function for a Point on the Tunnel Boundary

The Drucker–Prager failure criterion as a function of $\sigma_{y\infty}$, $A$, $B$, $k$, and $\Lambda$, can be written as:

$$-6P_0 - P_1 + \sqrt{3}\sqrt{(P_2 + P_3 + P_4 + P_5)} = 0 \tag{B1}$$

where:

$$P_0 = \frac{A}{\sigma_{y\infty}}$$
$$P_1 = 3B[2 + 4k + 4(1-k)\Lambda(1+\nu)\cos(2\theta)]$$
$$P_2 = 4(k-1)^2 + 6\left(1 + k^2\right)\Lambda^2$$
$$P_3 = -2(k-1)\Lambda[5 + 3\Lambda - 4\nu + k(1 + 3\Lambda + 4\nu)]\cos(2\theta) \tag{B2}$$
$$P_4 = (k-1)^2\Lambda^2(2 - 4\nu)^2\cos(2\theta)^2$$
$$P_5 = 6(k-1)^2\Lambda\cos(4\theta)$$

## Appendix C

### Calculation of $\Lambda_{duc}$

$\Lambda_{duc}$ is defined as the value of $\Lambda$ corresponding to ductile failure.

$$\Lambda_{duc} = \min[\min(\langle\Lambda_{duc,s}\rangle); \min(\langle\Lambda_{duc,c}\rangle)]$$

$$\langle\bullet\rangle = \text{positive part of } \bullet$$

$$\Lambda_{duc,s} = (T_1 \pm T_2)/T_3$$
$$\Lambda_{duc,c} = (T_4 \pm T_5)/T_6$$

where:

$$T_1 = 6AB(k-1)(\kappa-7) + (k-1)\sigma_{y\infty}[-1 - k(\kappa-7) + 6B^2(1+2k)(\kappa-7) + \kappa]$$

$$T_2 = \frac{1}{2}\sqrt{\Big\{4(k-1)^2[6AB(\kappa-7) + \sigma_{y\infty}(7k - 1 + 6B^2(1+2k)(\kappa-7) + \kappa - k\kappa)]^2 - 16\left[3A^2 + 6AB(1+2k)\sigma_{y\infty} + \left(-(k-1)^2 + 3(B+2Bk)^2\right){\sigma_{y\infty}}^2\right]\cdot \cdot\left[3B^2(k-1)^2(\kappa-7)^2 - (\kappa-1)^2 + 2k(\kappa-1)^2 + -k^2(13 + (-2+\kappa)\kappa)\right]\Big\}}$$

$$T_3 = \sigma_{y\infty}\left[3B^2(k-1)^2(\kappa-7)^2 - (\kappa-1)^2 + 2k(\kappa-1)^2 - k^2(13 + (-2+\kappa)\kappa)\right]$$

$$T_4 = 6AB(k-1)(\kappa-7) + (k-1)\sigma_{y\infty}\left[5 + k + 6B^2(1+2k)(\kappa-7) + \kappa - k\kappa\right]$$

$$T_5 = -\frac{1}{2}\sqrt{\Big\{-16\left[3A^2 + 6AB(1+2k)\sigma_{y\infty} + \left(-(k-1)^2 + 3(B+2Bk)^2\right){\sigma_{y\infty}}^2\right] \left[-13 + 3B^2(k-1)^2(\kappa-7)^2 + 2k(\kappa-1)^2 - k^2(\kappa-1)^2 - (-2+\kappa)\kappa\right] + 4(k-1)^2\left[6AB(\kappa-7) + \sigma_{y\infty}\left(5 + k + 6B^2(1+2k)(\kappa-7) + \kappa - k\kappa\right)\right]^2\Big\}}$$

$$T_6 = \sigma_{y\infty}\left[13 - 3B^2(k-1)^2(\kappa-7)^2 - 2k(\kappa-1)^2 + k^2(\kappa-1)^2 + (-2+\kappa)\kappa\right]$$

where $\kappa = 3 - 4\nu$ (Kolosov's constant).

## Appendix D

### Stress Induced in the Ellipse by Forces Distributed on Its Boundary

According to [73](Section 11.3), the stresses induced by a concentrated horizontal force ($F_x$) applied at the origin (with coordinates (0,0)) at a point defined by polar coordinates $(r, \theta)$ on a plate under plane strain conditions can be expressed as:

$$\sigma_{rr}^{(x)} = \frac{(3-2\nu)F_x\cos\theta}{4\pi(1-\nu)r}$$
$$\tau_{r\theta}^{(x)} = -\frac{(1-2\nu)F_x\sin\theta}{4\pi(1-\nu)r} \tag{D1}$$
$$\sigma_{\theta\theta}^{(x)} = -\frac{(1-2\nu)F_x\cos\theta}{4\pi(1-\nu)r}$$

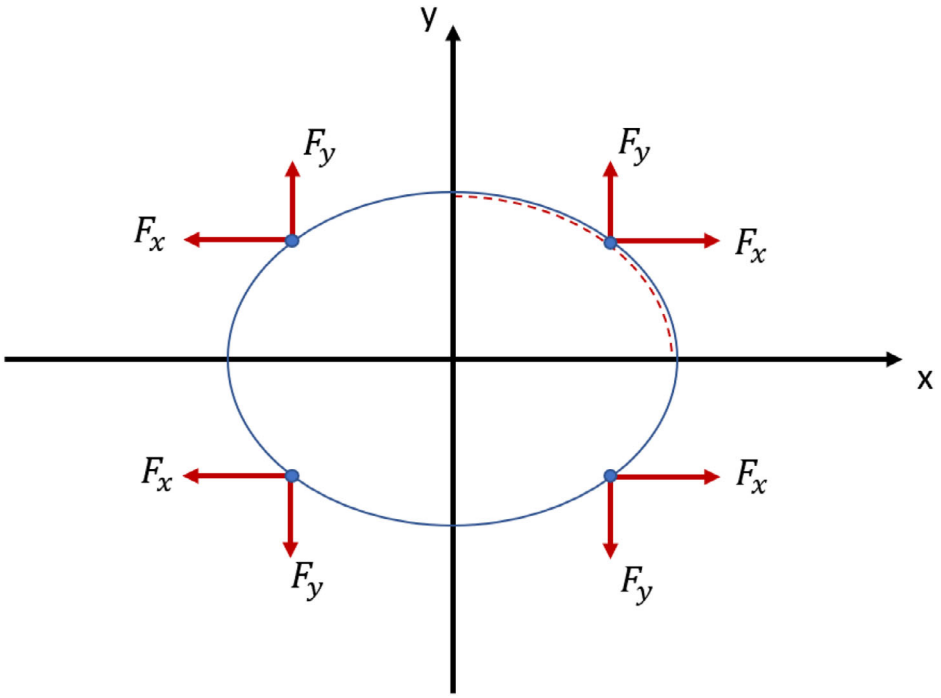


**FIGURE D1** | Four symmetrical points of the ellipse boundary considered in the computation.

where $\theta$ is measured from the $x$ axis, and a sign change is applied to reverse the sign convention used by Barber (positive tractions) and align it with that employed by Bažant et al. [52] and in the present study (positive compressions).

Hence, a concentrated vertical force $F_y$ at the origin induces stresses at the point with coordinates $(r, \theta)$:

$$\begin{aligned}\sigma_{rr}^{(y)} &= \frac{(3-2\nu)F_y \sin\theta}{4\pi(1-\nu)r}\\ \tau_{r\theta}^{(y)} &= \frac{(1-2\nu)F_y \cos\theta}{4\pi(1-\nu)r}\\ \sigma_{\theta\theta}^{(y)} &= -\frac{(1-2\nu)F_y \sin\theta}{4\pi(1-\nu)r}\end{aligned} \tag{D2}$$

obtained from Equation (D1) substituting $\theta$ with $\pi/2 - \theta$.

By changing the sign, the stresses induced by a concentrated inclined force with components $(F_x, F_y)$ at the point with coordinates $(r, \theta)$ are obtained at the origin. Passing to Cartesian coordinates, the stresses can be expressed as:

$$\begin{aligned}\sigma_{xx}^{(x)} &= \frac{\sigma_{rr}^{x}+\sigma_{\theta\theta}^{x}}{2} + \frac{\sigma_{rr}^{x}-\sigma_{\theta\theta}^{x}}{2}\cos(2\theta) - \tau_{r\theta}^{x}\sin(2\theta)\\ \sigma_{xx}^{(y)} &= \frac{\sigma_{rr}^{y}+\sigma_{\theta\theta}^{y}}{2} + \frac{\sigma_{rr}^{y}-\sigma_{\theta\theta}^{y}}{2}\cos(2\theta) - \tau_{r\theta}^{y}\sin(2\theta)\\ \sigma_{yy}^{(x)} &= \frac{\sigma_{rr}^{x}+\sigma_{\theta\theta}^{x}}{2} - \frac{\sigma_{rr}^{x}-\sigma_{\theta\theta}^{x}}{2}\cos(2\theta) + \tau_{r\theta}^{x}\sin(2\theta)\\ \sigma_{yy}^{(y)} &= \frac{\sigma_{rr}^{y}+\sigma_{\theta\theta}^{y}}{2} - \frac{\sigma_{rr}^{y}-\sigma_{\theta\theta}^{y}}{2}\cos(2\theta) + \tau_{r\theta}^{y}\sin(2\theta)\end{aligned} \tag{D3}$$

where all the stress components are functions of $r$ and $\theta$.

Now, let us examine four symmetrically positioned points along the boundary of the ellipse, where forces with symmetrical components $F_x$ and $F_y$ are applied, as illustrated in Figure D1. The resultant stress components at the center of the ellipse can be expressed as follows:

$$\begin{aligned}s_{xx}(r,\theta) &= 4\left[\sigma_{xx}^{(x)}(r,\theta) + \sigma_{xx}^{(y)}(r,\theta)\right]\\ s_{yy}(r,\theta) &= 4\left[\sigma_{yy}^{(x)}(r,\theta) + \sigma_{yy}^{(y)}(r,\theta)\right],\end{aligned} \tag{D4}$$

where $r, \theta$ are the polar coordinates of the point in the first quadrant of the Cartesian frame.

To determine the stress resulting from a distribution of forces applied along the entire boundary, these stress components need to be integrated over a quarter of the ellipse (as indicated by the dashed line in Figure D1).

The equation of the ellipse in parametric form is:

$$\begin{aligned}x(t) &= a\cos(t)\\ y(t) &= R\sin(t),\end{aligned} \tag{D5}$$

being $a$ and $R$ the ellipse semi axes and $t$ is the parameter. Accordingly, we rewrite $r$ and $\theta$ as a function of $t$:

$$\begin{aligned}r &= \sqrt{[a\cos(t)]^2 + [R\sin(t)]^2}\\ \theta &= \arctan\left(\frac{a\sin(t)}{R\cos(t)}\right)\end{aligned} \tag{D6}$$

The fictitious forces applied to the tunnel boundary are determined by the condition that they induce in the ellipse a stress $\boldsymbol{S}$ proportional to the original stress, diminished in accordance with the unloading parameter $\Lambda$:

$$\boldsymbol{S} = (1-\Lambda)\boldsymbol{\sigma}_{\infty} = \begin{bmatrix}(1-\Lambda)\sigma_{x\infty} & 0\\ 0 & (1-\Lambda)\sigma_{y\infty}\end{bmatrix} \tag{D7}$$

The forces $F_x$ and $F_y$ are determined by equating them to the tractions acting on the elliptical boundary. The outer normal at each point is

defined as follows:

$$\boldsymbol{n} = \{n_x, n_y\}$$

$$n_x = \frac{R\cos(t)}{\sqrt{[R\cos(t)]^2 + [a\sin(t)]^2}} \tag{D8}$$

$$n_y = \frac{a\sin(t)}{\sqrt{[R\cos(t)]^2 + [a\sin(t)]^2}}$$

so that the tractions $\boldsymbol{t}$ are:

$$\boldsymbol{t} = \{t_x, t_y\}$$

$$t_x = -\frac{R(\Lambda-1)\cos(t)\sigma_{x_\infty}}{\sqrt{R^2\cos(t)^2 + a^2\sin(t)^2}} \tag{D9}$$

$$t_y = -\frac{a(\Lambda-1)\sin(t)\sigma_{y_\infty}}{\sqrt{R^2\cos(t)^2 + a^2\sin(t)^2}}$$

At this juncture, the components $F_x$ and $F_y$ can be replaced with the elements of $\boldsymbol{t}$ in Equation (D4). Substituting Equation (D6) as well, the resulting expression is derived:

$$\begin{aligned} t_x(t) =& 2aR(1-\Lambda)\Big\{\cos(t)^2(3a^2 + R^2 - 2(a^2+R^2)\nu - \Big[(R^2(1-2\nu) \\ &+ a^2(2\nu-3)\cos(2t))\sigma_{x_\infty} + (a^2 - R^2 + 2(a^2+R^2)\nu \\ &+ (a^2 + R^2 + 2a^2\nu - 2R^2\nu)\cos(2t))\sin(t)^2\sigma_{y_\infty}\}/ \\ &[\pi(\nu-1)(a^2 + R^2 + (a^2-R^2)\cos(2t))^2]\Big] \\ t_y(t) =& \{2aR(1-\Lambda)[\cos(t)^2(a^2(2\nu-1) + R^2(1+2\nu) \\ &+ (a^2(2\nu-1) - R^2(1+2\nu))\cos(2t))\sigma_{x_\infty} \\ &+ (a^2 + 3R^2 - 2(a^2+R^2)\nu + (a^2(1-2\nu) + \\ &R^2(-3+2\nu))\cos(2t))\sin(t)^2\sigma_{y_\infty}\Big]\}/ \\ &\Big[\pi(\nu-1)(a^2 + R^2 + (a^2-R^2)\cos(2t))^2\Big] \end{aligned}$$

Subsequently, integration can be performed to compute the stresses induced within the ellipse:

$$T_{xx} = \int_0^{\pi/2} t_x(t)dt = -\frac{(\Lambda-1)(L_1+L_2)}{2(a+b)^2(\nu-1)}$$

$$T_{yy} = \int_0^{\pi/2} t_y(t)dt = \frac{(\Lambda-1)(L_3+L_4)}{2(a+b)^2(\nu-1)}$$

$$\begin{aligned} L_1 =& b[3a + 2b - 2(a+b)\nu]\sigma_{x_\infty} \\ L_2 =& a[-b + 2(a+b)\nu]\sigma_{y_\infty} \\ L_3 =& b[a - 2(a+b)\nu]\sigma_{x_\infty} \\ L_4 =& a[2a(\nu-1) + b(2\nu-3)]\sigma_{y_\infty} \end{aligned} \tag{D10}$$

Introducing the ellipse eccentricity $e = \frac{\sqrt{a^2-R^2}}{a}$, the expressions in Equation (D10) can be reformulated and expanded using Taylor's series with respect to $e$. Truncating the series at the second order, which is a valid approximation for small values of the ellipse eccentricity, yields a practical assumption applicable to deep tunnels. In fact, the depth of the splitting regions that form at the sides of a deep tunnel is generally much smaller than the diameter of the tunnel itself (hence the difference in length of the semi-axes of the ellipse that describes, according to this model, the enlarged cavity, is minimal). The approximate expressions are:

$$\begin{aligned} T_{xx} =& \frac{(\lambda-1)}{8(\nu-1)}\sigma_{y_\infty}\{1 - 5k - 4\nu(1-k) - e^2[\nu(k+1) - k]\} \\ T_{yy} =& \frac{(\lambda-1)}{8(\nu-1)}\sigma_{y_\infty}\{k - 5 + 4\nu(1-k) + e^2[\nu(k+1) - 1]\} \end{aligned} \tag{D11}$$

## Appendix E

### Calculation of the Eigenstrain $\epsilon$

The eigenstrain components correspond to the values of $\epsilon_x^*$, $\epsilon_y^*$ and $\epsilon_z^*$ which satisfy the system of equations shown in Equation (23), where the components of $\boldsymbol{\sigma}$ are calculated as shown in Equation (25):

$$\epsilon_x^* = -\frac{1}{8a^3E'}(C_1 + C_2 + C_3 + C_4)$$

$$\epsilon_y^* = \frac{1}{8a^2RE'}(D_1 + D_2 + D_3 + D_4)$$

$$\epsilon_z^* = -\frac{[k(\nu-1)+\nu]\sigma_{y_\infty}}{E'}$$

$$C_1 = 2R^3(\Lambda-1)(1+\nu)(k(\nu-1)+\nu)\sigma_{y_\infty}$$

$$C_2 = a(1+k)R^2(\Lambda-1)(\nu-1+2\nu^2)\sigma_{y_\infty}$$

$$C_3 = 2a^2R(1+\nu)[\Lambda-1+5\nu-5\Lambda\nu+k(-4-4\Lambda+5\nu+3\Lambda\nu)]\sigma_{y_\infty}$$

$$\begin{aligned} C_4 =& a^3\{8(-1+\nu^2)\sigma_{cr} + [1+7\Lambda-k(3+5\Lambda)]\sigma_{y_\infty} + \\ &\nu[3-3\Lambda-6\nu-10\Lambda\nu+k(7+\Lambda+6(\Lambda-1)\nu)]\sigma_{y_\infty}\} \end{aligned}$$

$$D_1 = 2aR^2(\Lambda-1)(1+\nu)(\nu-1+k\nu)\sigma_{y_\infty}$$

$$D_2 = (1+k)R^3(\Lambda-1)(\nu-1+2\nu^2)\sigma_{y_\infty}$$

$$\begin{aligned} D_3 =& a^2R[8(-1+\nu^2)\sigma_{cr} + \sigma_{y_\infty} + 7\Lambda\sigma_{y_\infty} - \\ &k(3+5\Lambda)\sigma_{y_\infty} - (\Lambda-1)\nu(3+10\nu)\sigma_{y_\infty} + k\nu(-9+\Lambda+10\nu+6\Lambda\nu)\sigma_{y_\infty}] \end{aligned}$$

$$D_4 = 2a^3(1+\nu)\{8(\nu-1)\sigma_{cr} + [2+6\Lambda-3\nu-5\Lambda\nu+k(\Lambda-1)(3\nu-1)]\sigma_{y_\infty}\}$$

## Appendix F

### Variation of the Potential Energy $\Delta\Pi_1$

The expression of the potential energy variation caused by the gradual excavation of an elliptic cavity from an infinite elastic body ($\Omega$), considering surface tractions on the elliptic boundary corresponding to $\sigma_{cr}$, was obtained using Equation (27). While performing this operation, the substitutions shown in Equation (28) were made.

$$\Delta\Pi_1 = -\frac{\pi(A_1+A_2+A_3+A_4+A_5+A_6+A_7)}{128a^4E'(\nu-1)}$$

$$A_1 = -aR^5(\Lambda-1)^2(1-2\nu)^2(1+\nu)(\sigma_{x_\infty} + \sigma_{y_\infty})^2$$

$$A_2 = -2R^6(\Lambda-1)^2(1+\nu)((\nu-1)\sigma_{x_\infty} + \nu\sigma_{y_\infty})^2$$

$$\begin{aligned} A_3 =& -2a^3R^3(\Lambda-1)(\nu-1+2\nu^2)(\sigma_{x_\infty} + \sigma_{y_\infty})[(-3-5\Lambda+2\nu+6\Lambda\nu)\sigma_{x_\infty} \\ &+(1+7\Lambda+2\nu-10\Lambda\nu)\sigma_{y_\infty}] \end{aligned}$$

$$\begin{aligned} A_4 =& 2a^6(1+\nu)[8(\nu-1)\sigma_{cr} + (\Lambda-1)(3\nu-1)\sigma_{x_\infty} + (2+6\Lambda-3\nu-5\Lambda\nu)\sigma_{y_\infty}] \\ &\times[8(\nu-1)\sigma_{cr} - (\Lambda-1)(3\nu-1)\sigma_{x_\infty} + (-2-6\Lambda+3\nu+5\Lambda\nu)\sigma_{y_\infty}] \end{aligned}$$

$$\begin{aligned} A_5 =& -2a^2R^4(\Lambda-1)(1+\nu)[(8+9(-2+\nu)\nu + \Lambda(8+7(-2+\nu)\nu))\sigma_{x_\infty}^2 \\ &-2(\Lambda-1-9(\nu-1)\nu + \Lambda(\nu-1)\nu)\sigma_{x_\infty}\sigma_{y_\infty} - (\Lambda-1)(-1+9\nu^2)\sigma_{y_\infty}^2] \end{aligned}$$

$$A_6 = a^5R[(-73 - \Lambda^2(5-6\nu)^2(1+\nu) - 2\Lambda(1+\nu)(-3+2\nu)(-5+6\nu)$$

$$+\nu(195+4\nu(-46+15\nu)))\sigma_{x\infty}^2+2(3+\Lambda^2(1+\nu)(-5+6\nu)(-7+10\nu)$$
$$+2\Lambda(1+\nu)(13+4(-5+\nu)\nu)+\nu(71+4\nu(-32+15\nu)))\sigma_{x\infty}\sigma_{y\infty}$$
$$-(1+\Lambda^2(7-10\nu)^2(1+\nu)-2\Lambda(1+\nu)(1+2\nu)(-7+10\nu)$$
$$+\nu(5+12(6-5\nu)\nu))\sigma_{y\infty}^2]$$

$$A_7 = 2a^4R^2(1+\nu)[-((16(1+\Lambda)^2-2\big(21+\Lambda(30+13\Lambda)\big)\nu$$
$$+(31+3\Lambda(6+5\Lambda))\nu^2)\sigma_{x\infty}^2)+2(\Lambda-1)\big(5+31(\nu-1)\nu$$
$$+\Lambda(3+\nu(-25+17\nu)))\sigma_{x\infty}\sigma_{y\infty}-(\Lambda-1)\big(-5+(20-31\nu)\nu$$
$$+\Lambda(-11+3\nu(4+5\nu))\big)\sigma_{y\infty}^2]$$

## Appendix G

## Complete Variation of the Potential Energy $\Delta\Pi_0$

$$\Delta\Pi_0 = \frac{1}{16E'(\nu-1)}\pi R^2(B_1+B_2+B_3)$$

$$B_1 = \big\{11-2\Lambda(1+\nu)(-5+8\nu)+\nu(-29+24\nu)+\Lambda^2(1+\nu)$$
$$\times\big[11+8\nu(-3+2\nu)\big]\big\}\sigma_{x\infty}^2$$

$$B_2 = -2\big\{-1+(15-16\nu)\nu+2\Lambda(1+\nu)$$
$$+\Lambda^2(1+\nu)\big[7+8\nu(-3+2\nu)\big]\big\}\sigma_{x\infty}\sigma_{y\infty} \quad \text{(G1)}$$

$$B_3 = \big\{3+\nu(-5+8\nu)-2\Lambda(1+\nu)(-5+8\nu)$$
$$+\Lambda^2(1+\nu)\big[11+8\nu(-3+2\nu)\big]\big\}\sigma_{y\infty}^2$$

## Appendix H

## Variation of the Energy Due to Splitting Cracks, $\Delta\Pi$

$$\Delta\Pi = \frac{1}{128(E'-E'\nu^2)}\pi[H_1+H_2(H_3+H_4+H_5)]$$

$$H_1 = -\frac{1}{9R^4w^4\lambda^2}4h^2(2a-R)(a+R)\cdot\big(12G_iR^2w^2+h\pi^2E'\lambda\big)^2\big(-1+\nu^2\big)$$

$$H_2 = \frac{1}{a^4(\nu-1)}(a-R)$$

$$H_3 = \big\{2a^5(\Lambda-1)^2(1-3\nu)^2(1+\nu)-2R^5(\Lambda-1)^2(\nu-1)^2(1+\nu)$$
$$-aR^4(\Lambda-1)^2(1+\nu)\big(3-8\nu+6\nu^2\big)-a^3R^2(-1+\Lambda)(1+\nu)$$
$$\times\big[19+4\nu(-11+5\nu)+\Lambda\big(29-68\nu+44\nu^2\big)\big]$$
$$+a^4R\big[75+\nu\big(-205+2(95-21\nu)\nu\big)+9\Lambda^2(1+\nu)\big(3-8\nu+6\nu^2\big)$$
$$-2\Lambda(1+\nu)(-13+2\nu(8+3\nu))\big]-a^2R^3(\Lambda-1)(1+\nu)$$
$$\times\big[13+4\nu(-7+3\nu)+\Lambda(19+4\nu(-9+5\nu))\big]\big\}\sigma_{x\infty}^2$$

$$H_4 = -2\big\{2R^5(\Lambda-1)^2\nu\big(-1+\nu^2\big)+a^2R^3(\Lambda-1)\cdot(1+\nu)$$
$$\times\big[1-\Lambda-4(3+\Lambda)\nu+4(3+\Lambda)\nu^2\big]+aR^4(\Lambda-1)^2\big(1-5\nu+6\nu^3\big)$$
$$+a^3R^2(\Lambda-1)\big[3-3\Lambda+(-17+\Lambda)\nu-4(-5+\Lambda)\nu^3\big]$$
$$+2a^5(\Lambda-1)(1+\nu)(3\nu-1)\big[-2+3\nu+\Lambda(-6+5\nu)\big]$$
$$+a^4R\big[-1-2\Lambda(1+\nu)(-9+2\nu(3+\nu))$$
$$+\Lambda^2(1+\nu)(47+6\nu(-23+15\nu))+\nu(85+2\nu(-64+21\nu))\big]\big\}\sigma_{x\infty}\sigma_{y\infty}$$

$$H_5 = \big\{-2R^5(\Lambda-1)^2\nu^2(1+\nu)-aR^4(\Lambda-1)^2(1+\nu)\big(1-4\nu+6\nu^2\big)$$
$$+a^2R^3(\Lambda-1)^2(1+\nu)\big[-3+4\nu(1+3\nu)\big]$$
$$+2a^5(1+\nu)[-2+3\nu+\Lambda(-6+5\nu)]^2$$
$$+\Lambda^2(1+\nu)(121+10\nu(-26+15\nu))\big]\big\}\sigma_{y\infty}^2$$

## Appendix I

## Complete Expressions of the Left and Right Sides of Equation (32)

$$\frac{\partial\Delta W_f}{\partial a} = \frac{G_f\pi R}{h}$$

$$-\frac{\partial\Delta\Pi}{\partial a} = -\frac{1}{128Yp}\pi(F_1+F_2+F_3+F_4+F_5+F_6+F_7)$$

$$F_1 = 64R\left(\frac{h^2\pi^2E'}{12R^2w^2}+\frac{G_ih}{\lambda}\right)^2$$

$$F_2 = \frac{3R^5(\Lambda-1)^2(1-2\nu)^2\big(\sigma_{x\infty}+\sigma_{y\infty}\big)^2}{a^4(\nu-1)^2}$$

$$F_3 = \frac{8R^6(\Lambda-1)^2\big((\nu-1)\sigma_{x\infty}+\nu\sigma_{y\infty}\big)^2}{a^5(\nu-1)^2}$$

$$F_4 = \frac{1}{a^2(\nu-1)^2}2R^3\cdot(\Lambda-1)(2\nu-1)\cdot\big(\sigma_{x\infty}+\sigma_{y\infty}\big)$$
$$\times\big[\big(-3+2\nu+\Lambda(-5+6\nu)\big)\sigma_{x\infty}+\big(1+\Lambda(7-10\nu)+2\nu\big)\sigma_{y\infty}\big]$$

$$F_5 = \frac{1}{(\nu-1)^2}4a\big[8(\nu-1)\sigma_{cr}+(\Lambda-1)(3\nu-1)\sigma_{x\infty}$$
$$+(2+6\Lambda-3\nu-5\Lambda\nu)\sigma_{y\infty}\big]\cdot\big[8(\nu-1)\sigma_{cr}+(\Lambda-1+3\nu-3\Lambda\nu)\sigma_{x\infty}$$
$$+(-2-6\Lambda+3\nu+5\Lambda\nu)\sigma_{y\infty}\big] \quad (50)$$

$$F_6 = \frac{1}{a^3(\nu-1)^2}4R^4(\Lambda-1)\,8+9(-2+\nu)\nu+\Lambda(8+7(-2+\nu)\nu)]\sigma_{x\infty}^2$$
$$-2[\Lambda-1-9(\nu-1)\nu+\Lambda(\nu-1)\nu]\sigma_{x\infty}\sigma_{y\infty}-(\Lambda-1)\cdot\big(-1+9\nu^2\big)\sigma_{y\infty}^2\}$$

$$F_7 = \frac{1}{(\nu-1)^2(1+\nu)}R\{[-73-\Lambda^2(5-6\nu)^2(1+\nu)$$
$$-2\Lambda(1+\nu)(-3+2\nu)(-5+6\nu)+\nu(195+4\nu(-46+15\nu))]\sigma_{x\infty}^2$$
$$+2[3+\Lambda^2(1+\nu)(-5+6\nu)(-7+10\nu)+2\Lambda(1+\nu)(13+4(-5+\nu)\nu)$$
$$+\nu(71+4\nu(-32+15\nu))]\sigma_{x\infty}\sigma_{y\infty}-[1+\Lambda^2(7-10\nu)^2(1+\nu)$$
$$-2\Lambda(1+\nu)(1+2\nu)(-7+10\nu)+\nu(5+12(6-5\nu)\nu)]\sigma_{y\infty}^2\}$$

## Appendix J

## Complete Expression of $\sigma_{ef}^2$

$$\sigma_{ef}^2 = \frac{1}{8(\nu-1)^2(1+\nu)}(J_1+J_2+J_3)$$

$$J_1 = \big\{13-3(-2+\Lambda)\Lambda-31\nu$$
$$+(-2+\Lambda)\Lambda\nu+4[5+(-2+\Lambda)\Lambda]\nu^2\big\}\sigma_{x\infty}{}^2$$

$$J_2 = -2\big\{-1+(15-16\nu)\nu+2\Lambda(1+\nu)$$
$$+\Lambda^2(1+\nu)[7+8\nu(-3+2\nu)]\big\}\sigma_{x\infty}\sigma_{y\infty}$$

$$J_3 = \big\{1+3\nu(-1+4\nu)-2\Lambda(1+\nu)(-7+12\nu)$$
$$+\Lambda^2(1+\nu)[25+4\nu(-13+8\nu)]\big\}\sigma_{y\infty}{}^2 \quad \text{(J1)}$$

## Appendix K

### Expressions of $\Lambda_{brt}$

$$\Lambda_{brt} = \min(\langle \Lambda_{brt,c} \rangle)$$

$$\langle \bullet \rangle = \text{positive part of } \bullet$$

$$\Lambda_{brt,c} = \left( N_1 \pm \frac{1}{2} \sqrt{N_2 \cdot N_3 \cdot N_4} \right) / N_5$$

$$N_1 = [7 + k(-2 + 3k)]\sigma_{y\infty} - [5 + k(2 + k)]\nu\sigma_{y\infty} - 4\left(3 + k^2\right)\nu^2\sigma_{y\infty}$$

$$N_2 = 4(1 + \nu)^2 \left\{ -7 + 12\nu + k\left[2 + k(-3 + 4\nu)\right] \right\}^2 \sigma_{y\infty}^2 - 32\left(-1 + \nu^2\right)^2$$

$$N_3 = 25 - 14k - 3k^2 + 4(-1 + k)(13 + k)\nu - 32(-1 + k)\nu^2$$

$$N_4 = -3 \cdot 5^{1/3} \left( \frac{G_i G_f E}{\lambda - \lambda\nu^2} \right)^{2/3} + \\ + \frac{\left\{ 1 + 2k + 13k^2 - [3 + k(30 + 31k)]\nu + 4(1 + k)(3 + 5k)\nu^2 \right\} \sigma_{y\infty}^2}{8(\nu - 1)^2(1 + \nu)}$$

$$N_5 = (1 + \nu)\left[ -25 + 14k + 3k^2 - 4(-1 + k)(13 + k)\nu + 32(-1 + k)\nu^2 \right] \sigma_{y\infty}$$